

Viscosity of anhydrous and hydrous peridotite melts

Danilo Di Genova^{1,2}, Dmitry Bondar¹, Alessio Zandonà^{3,4,*}, Pedro Valdivia¹, Raschid Al-Mukadam⁵, Hongzhan Fei¹, Anthony C. Withers¹, Tiziana Boffa Ballaran¹, Alexander Kurnosov², Catherine McCammon¹, Joachim Deubener⁵, Tomoo Katsura¹

¹Bayerisches Geoinstitut, University of Bayreuth, Universitätsstraße 30, 95440, Bayreuth, Germany

²Institute of Environmental Geology and Geoengineering, National Research Council of Italy, Rome, Italy

³CNRS, CEMHTI UPR3079, Univ. Orléans, F-45071 Orléans, France

⁴Friedrich-Alexander-Universität Erlangen-Nürnberg, Department of Materials Science (Glass and Ceramics), Martensstr. 5, 91058 Erlangen, Germany

⁵Institute of Non-metallic Materials, Clausthal University of Technology, Zehntnerstraße 2a, D-38678 Clausthal-Zellerfeld, Germany

*Corresponding authors: alessio.zandona@fau.de

Abstract

The melt viscosity (η) of anhydrous and hydrous peridotite was investigated using a multipronged approach combining micropenetration viscometry, conventional DSC, flash DSC and Brillouin spectroscopy. Raman spectroscopy measurements were used to verify the absence of crystallization and/or degassing during high-temperature measurements of these extremely reactive glasses and melts, ensuring that the data corresponded to the crystal-free melt viscosity. Based on the experimental data, an accurate description of the viscosity of peridotite melts over thirteen orders of magnitude (from T_g to $\eta \approx 10^{-1}$ Pa s) is provided in a broad range of compositions and oxidation states. Since empirical models predict viscosities that can significantly deviate from measured data to varying degrees, a new model was developed for the temperature- and H₂O-dependent viscosity of peridotite melts (up to 12 mol% H₂O content).

Keywords: peridotite melt; viscosity; glass transition; calorimetry; Brillouin spectroscopy

30 1. Introduction

31 Magmatic activity is a daily occurrence on Earth (Loughlin et al., 2015). The lavas that are
32 produced have a wide variety of compositions (Keller and Krafft, 1990; Lipman and Mullineaux,
33 1981; Mahood and Hildreth, 1986; Pirrung et al., 2003; Sigurdsson et al., 1982; Sigurdsson and
34 Carey, 1989; Walker et al., 1984), extending from extremely SiO₂-rich rhyolites to carbonatites.
35 Chemical composition (including volatile content) ultimately determines the intrinsic viscoelastic
36 properties of magmas and the tendency to partially crystallize and degas, so that it represents a
37 crucial parameter controlling the eruptive styles of volcanoes (Gonnermann and Manga, 2013).
38 Among those parameters that govern both magma transport from the reservoir to the volcanic vent
39 and eruptive style, viscosity is arguably the most important (Cassidy et al., 2018; Di Genova et al.,
40 2017a). Indeed, volcanologists have long pursued the experimental investigation of melt viscosity
41 as a function of temperature and composition (e.g., Ishibashi and Sato, 2007; Kolzenburg et al.,
42 2018; Whittington et al., 2009), as well as its subsequent numerical modelling by different
43 approaches including classical linear regression and machine learning (Giordano et al., 2008; Hui
44 and Zhang, 2007; Langhammer et al., 2022). The extent and quality of the dataset used to develop
45 these models directly affect the reliability of their predictions, so that one should strive for a
46 detailed experimental exploration of the largest possible compositional landscape. Unfortunately,
47 there are undeniable experimental challenges related to the viscosity measurements of volcanic
48 melts (or their synthetic analogs), namely: (i) their undercooling-driven tendency to crystallize,
49 which typically limits concentric-cylinder low-viscosity ($\sim 10^4$ – 10^2 Pa s) determinations (e.g.,
50 Kolzenburg et al., 2018) to superliquidus temperatures and only mild undercooling; (ii) the prompt
51 degassing of volatile-bearing melts at ambient pressure, which can be only overcome through
52 falling-sphere experiments and the application of confining pressure (e.g., Liebske et al., 2005),

53 with significant technical difficulties; (iii) the limited glass-forming ability of volcanic
54 compositions, since glassy samples are necessary for high-viscosity (10^{12} – 10^6 Pa s) measurements
55 by micropenetration (e.g., Di Genova et al., 2020b), parallel-plate deformation (e.g., Whittington
56 et al., 2009), beam bending (e.g., Hagy, 1963) or fiber elongation (e.g., Taniguchi, 1992)
57 viscometry. Moreover, even when the required glassy samples can be synthesized, their limited
58 stability during high-temperature measurements has been repeatedly demonstrated by postmortem
59 measurements using Raman spectroscopy and high-resolution imaging (Di Genova et al., 2020b,
60 2017a; Kleest et al., 2020; Liebske et al., 2003a; Scarani et al., 2022): nanocrystallization of Fe-
61 Ti-oxides can affect sample homogeneity and alter the composition of the residual melt, preventing
62 derivation of the crystal-free viscosity. As a consequence, currently available viscosity models
63 (Giordano et al., 2008; Hui and Zhang, 2007; Langhammer et al., 2022) have been trained in a
64 relatively restricted volcanological domain of temperature and chemistry, with questionable
65 applicability to compositional extremes such as ultrabasic melts and very H₂O-rich matrices.

66 To overcome these limitations, we designed this work as a targeted investigation of melts
67 that locate substantially outside the range of previously analyzed compositions, considering an
68 unprecedented range of anhydrous and hydrous viscosities and testing the predictive performance
69 of numerical viscosity models available in the literature (Giordano et al., 2008; Hui and Zhang,
70 2007; Langhammer et al., 2022). We therefore selected anhydrous and hydrous peridotite liquids:
71 the viscosity of these materials was investigated only sporadically so far (Dingwell et al., 2004;
72 Liebske et al., 2005) due to their extreme features, namely a SiO₂ content < 50 wt% that leads to
73 extreme structural depolymerization and a very strong tendency to undercooling-driven
74 crystallization. However, ultramafic liquids play a key role for our understanding of deep mantle
75 dynamics and for planetary formation theories: the Earth is thought to have experienced a large

76 degree of melting during planetary accretion, as well as after the giant impact that originated the
77 Moon (e.g., Nakajima and Stevenson, 2015; Ohtani, 1985). The resulting peridotite magma oceans
78 facilitated core formation through silicate-metal segregation (e.g., Li and Agee, 1996; Wade and
79 Wood, 2005) and originated the atmosphere and hydrosphere through degassing (e.g., Karato et
80 al., 2020; Sossi et al., 2020). Moreover, high-pressure experiments demonstrated that highly
81 ultramafic and Mg-rich melts (such as picrites and kimberlites) could be formed at present by
82 partial melting of peridotite in the upper and lower mantle (e.g., Fei, 2021; Kawamoto and
83 Holloway, 1997; Mysen and Boettcher, 1975; Sinmyo et al., 2019), with far-reaching implications
84 for the transport of incompatible elements such as hydrogen (Karato et al., 2020).

85 For the synthesis of anhydrous ultrabasic melts and glasses, we relied on aerodynamic
86 levitation coupled with laser heating (Hennet et al., 2011; Weber, 2010) which facilitates glass
87 formation by suppressing heterogeneous surface nucleation due to its containerless conditions; in
88 the case of hydrous peridotite melts, we employed a recently developed rapid-quench multi-anvil
89 technique (Bondar et al., 2021, 2020). Due to the occasionally very low amounts of available
90 material (especially for hydrous samples), we studied melt viscosity using a multipronged
91 experimental approach (see Section 1.1) carefully combining classical viscometry with standard
92 and flash calorimetry and Brillouin spectroscopy, whose applicability is here tested and
93 demonstrated to be successful also for such extreme compositions. On the whole, our results
94 provide the first quantitative parameterization of peridotite melt viscosity as a function of
95 temperature, overall composition (e.g., FeO_{tot}) and water content (up to 12 mol%).

96

97 *1.1. Deriving and modelling melt viscosity*

98 The experimental procedure applied in this work has been presented, tested and optimized
99 in previous studies (Cassetta et al., 2021; Di Genova et al., 2020b; Scarani et al., 2022; Stabile et
100 al., 2021); its cornerstones are briefly summarized here. We have demonstrated that the
101 combination of calorimetry (DSC) and Brillouin spectroscopy (BLS) enables the modelling of melt
102 viscosity as a function of temperature [$\eta(T)$] (Cassetta et al., 2021). We model $\eta(T)$ using the three-
103 parameter MYEGA equation (Eq. 1) (Mauro et al., 2009b):

104

$$105 \quad \log_{10}\eta(T) = \log_{10}\eta_{\infty} + (12 - \log_{10}\eta_{\infty}) \frac{T_g}{T} \exp \left[\left(\frac{m}{12 - \log_{10}\eta_{\infty}} - 1 \right) \left(\frac{T_g}{T} - 1 \right) \right] \quad (1)$$

106

107 where $\log_{10}\eta_{\infty}$ is the viscosity at infinite temperature (Langhammer et al., 2021; Zheng et al., 2011),
108 T_g is the glass transition temperature [$\eta(T_g) = 10^{12}$ Pa s] and m is the melt fragility (Eq. 2) (Angell,
109 1995):

110

$$111 \quad m = \left. \frac{\partial \log_{10}\eta}{\partial T_g/T} \right|_{T=T_g} \quad (2)$$

112

113 The existence of a universal, chemically invariant limit of viscosity at infinite temperature
114 constitutes a long-standing concept, already elaborated using other parameterizations such as the
115 Adam-Gibbs (AG) or the Vogel–Fulcher–Tammann–Hesse (VFTH) equations (Persikov, 1991;
116 Russell et al., 2003, 2002). For the MYEGA equation, this value was calibrated to $\log_{10}\eta_{\infty} = -2.93$
117 ± 0.3 for silicate melts of volcanological and technological interest (Langhammer et al., 2021;
118 Zheng et al., 2011). Notably, this value is close to the lowest viscosity values measured at high

119 temperatures in silicate and carbonatite melts (Di Genova et al., 2016a; Dingwell et al., 2022;
120 Dobson et al., 1996; Kono et al., 2014; Persikov et al., 2017; Stagno et al., 2018). By fixing this
121 value, only T_g and m are required to parameterize $\log_{10}\eta(T)$.

122 The melt fragility m was derived spectroscopically from BLS measurements performed on
123 glasses at room temperature (Cassetta et al., 2021) because this approach avoids the need to acquire
124 viscosity data over an extended temperature range, which is challenging or impossible for poor
125 glass-forming liquids (Di Genova et al., 2020b; Kleest et al., 2020; Liebske et al., 2003b; Richet
126 et al., 1996; Scarani et al., 2022). Fragility m was obtained as (Eq. 3):

127

$$128 \quad m = 43.429 \cdot \frac{K}{G} - 31.871 \quad (3)$$

129

130 where K/G is the elastic moduli ratio calculated (Eq. 4) using the measured shear v_s and
131 longitudinal v_p sound velocities (Cassetta et al., 2021):

132

$$133 \quad \frac{K}{G} = \left(\frac{v_p}{v_s}\right)^2 - \frac{4}{3} \quad (4)$$

134

135 For samples of sufficient size and exhibiting enough glass stability to be measured by DSC (here,
136 anhydrous peridotite glasses), we derived T_g via DSC. The DSC approach to derive T_g builds on
137 the relationship (Eq. 5) provided by (Scherer, 1984):

138

$$139 \quad \log_{10}\eta(T_f) = K - \log_{10}(q_h) \quad (5)$$

140

141 where q_h is the heating rate in K s^{-1} employed during the DSC measurement and T_f is the fictive
 142 temperature in Kelvin, at which the structure and properties (e.g., volume and enthalpy) of the
 143 glass equal those of the corresponding undercooled liquid at the same temperature (Mauro et al.,
 144 2009a). The addend K is the chemically invariant shift factor (Al-Mukadam et al., 2021a, 2021b,
 145 2020; Di Genova et al., 2020b; Stabile et al., 2021; Yue et al., 2002). Because we used the DSC
 146 approach involving matching heating and cooling rates (see methodology), here T_f corresponds to
 147 T_{onset} (Fig. 1) (Al-Mukadam et al., 2020; Di Genova et al., 2020b). As such, Eq. 5 can be written
 148 as (Eq. 6) :

149

$$150 \quad \log_{10}\eta(T_{onset}) = K_{onset} - \log_{10}(q_h) \quad (6)$$

151

152 where $K_{onset} = 11.20 \pm 0.15$ (Di Genova et al., 2020b; Stabile et al., 2021). Therefore, when $q_h =$
 153 10 K min^{-1} (0.17 K s^{-1}), one has $\eta(T_{onset}) \approx 10^{12} \text{ Pa s}$ and thus $T_{onset} \equiv T_g$, which can be directly
 154 inserted into the MYEGA equation to obtain a full viscosity parameterization without the need of
 155 data fitting ($\log_{10}\eta_\infty = -2.93 \pm 0.3$ and m is obtained spectroscopically). In such cases, the
 156 agreement with experimental viscosity data obtained by micropenetration viscometry or additional
 157 DSC measurements performed at different q_h can be used to validate this approach. Additionally,
 158 several studies (Stabile et al., 2021 and references therein) demonstrated that with Eq. 5 one can
 159 also derive the melt viscosity at T_{peak} (Fig. 1) of the heat flow (Eq. 7):

160

$$161 \quad \log_{10}\eta(T_{peak}) = K_{peak} - \log_{10}(q_h) \quad (7)$$

162

163 where $K_{peak} = 9.84 \pm 0.20$ (Di Genova et al., 2020b; Stabile et al., 2021).

164 The hydrous samples synthesized by the rapid-quench multi-anvil technique (Bondar et al.,
165 2022) are too unstable and small to be characterized by conventional DSC or viscometry. Their
166 viscosity can therefore be derived through rate-matching flash DSC measurements in the range
167 $10^{9.2}$ - $10^{6.4}$ Pa s, subsequently fitting the value of T_g in Eq. 1 using these data points ($\log_{10}\eta_\infty =$ -
168 2.93 ± 0.3 and m is obtained spectroscopically).

169

170 2. Materials and methods

171 2.1. Peridotite glass synthesis

172 Anhydrous and hydrous glasses are identified by a nomenclature mirroring their chemical
173 composition, namely: S_F_W_, where S and F respectively stand for the SiO₂ and FeO_{tot} molar
174 contents of the base anhydrous glass and W for the H₂O molar content. This choice enables
175 straightforward identification of samples with a similar anhydrous base composition, but different
176 water contents. Anhydrous glasses were synthesized in containerless conditions at the CEMHTI
177 laboratory in Orléans (France), using the aerodynamic levitation device coupled to laser heating
178 (ADL) detailed elsewhere (Zandona et al., 2022). The device consists of two CO₂ lasers
179 (wavelength: 10.6 μ m; maximum power: 250 W) heating from above and below a sample weighing
180 a few tens of milligrams and suspended in a copper nozzle by a gas jet (Ar or O₂).

181 For the syntheses, laboratory-grade SiO₂ (99.9%, Chempur), Al₂O₃ (99.999%, Strem
182 Chemicals), MgO (99.5%, Strem Chemicals), FeO (99.9%, Aldrich), Fe₂O₃ (68.2-71.7 %Fe,
183 Sigma-Aldrich) and CaCO₃ (99.95%, Strem Chemicals) were weighed in the right proportions,
184 mixed thoroughly in an agate mortar with the addition of ethanol, dried, and compacted with a
185 hydraulic press into cylindrical pellets of approximately 1 g. Small chunks of these pellets were
186 then introduced into the ADL nozzle and melted by quickly ramping up the laser power until full

187 liquefaction of the materials was achieved, at pyrometer readings (wavelength: 0.9 μm) in the
188 range 1800 – 2100 $^{\circ}\text{C}$ depending on composition. After holding at the maximum temperature for
189 ~5 s for homogenization, the melts were quenched into glasses by instantaneously shutting off the
190 lasers, which typically yields cooling rates in the order of a few hundreds of kelvins per second.
191 No signs of high-temperature volatilization (smoke or material deposition on the nozzle wall) were
192 detected using this procedure. Samples were synthesized using FeO as raw material and Ar as a
193 levitation gas. To explore the effect of different oxy-reduction conditions, two samples (S44F6+
194 and S44F12+) were obtained using Fe_2O_3 in the starting powder mixtures and pure O_2 as a
195 levitation gas.

196 The set of four hydrous peridotite glasses was previously synthesized at confining pressure
197 of 0.9 GPa using a 15-MN Kawai-type multi-anvil press equipped with a novel rapid-quench multi-
198 anvil technique (Bondar et al., 2021, 2020). The detailed description and synthesis conditions of
199 glasses S38F5W1, S40F5W6, S43F7W8 and S39F6W12 (referred to as I1075, I1045, I867 and
200 I1111, respectively, in the previous study) are given in (Bondar et al., 2022).

201

202 2.2. *Electron microprobe analyses*

203 Major element compositions of glasses were determined using a JEOL JXA-8200 electron
204 probe microanalyzer equipped with five wavelength-dispersive spectrometers at the Bayerisches
205 Geoinstitut (BGI), University of Bayreuth (Germany). Samples were carbon-coated with a
206 thickness of 12 nm before analysis. Oxygen was calculated by stoichiometry, and all the iron was
207 assigned as ferrous iron. Glasses were analyzed with a defocused 10 μm beam using 15 kV
208 accelerating voltage, 5 nA beam current, a peak counting time of 20 s and a background counting
209 time of 10 s. Measured peak counts were corrected using the PRZ (Phi-Rho-Z) method

210 (Armstrong, 1991). Standards included wollastonite (Si, Ca), hematite (Fe), periclase (Mg), spinel
 211 (Al), albite (Na), orthoclase (K), manganese titanate (Ti, Mn), and chromium metal (Cr). Results
 212 of the analyses are reported in Tab. 1.

213

214 *Table 1. Chemical composition (mol%) of samples used and considered in this study. Uncertainties are reported in parenthesis for*
 215 *each value. References: *this study, ¹(Bondar et al., 2022), ²(Bondar, 2023), ³(Dingwell et al., 2004). Water contents in H₂O-*
 216 *bearing glasses were determined by a combination of elastic recoil detection analysis and secondary ion mass spectrometry*
 217 *(Bondar, 2023).*

Sample	SiO ₂	TiO ₂	Al ₂ O ₃	FeO _{tot}	MnO	MgO	CaO	Na ₂ O	K ₂ O	P ₂ O ₅	Cr ₂ O ₃	H ₂ O	Fe ³⁺ /Fe _{tot}	Ref.
S44F0	44.16 (0.15)	0.02 (0.02)	3.39 (0.04)	0.05 (0.02)	0.01 (0.01)	45.68 (0.17)	6.64 (0.12)	0.02 (0.02)	0.01 (0.01)	0.02 (0.02)	n.a.	b.d.l. ^a	-	*
S44F6+	43.67 (0.21)	0.01 (0.01)	3.37 (0.05)	6.19 (0.12)	0.01 (0.01)	40.05 (0.22)	6.63 (0.12)	0.03 (0.02)	0.02 (0.01)	b.d.l.	n.a.	b.d.l. ^a	0.54 (0.05)	*
S44F6	43.28 (0.20)	0.01 (0.01)	3.43 (0.06)	6.40 (0.11)	0.01 (0.01)	40.32 (0.17)	6.49 (0.10)	0.02 (0.02)	0.02 (0.01)	0.01 (0.01)	n.a.	b.d.l. ^a	0.38 (0.05)	*
S44F12+	43.11 (0.17)	0.02 (0.02)	3.36 (0.05)	12.10 (0.14)	0.01 (0.01)	34.65 (0.20)	6.70 (0.10)	b.d.l.	0.02 (0.01)	0.02 (0.02)	n.a.	b.d.l. ^a	0.50 (0.05)	*
S44F12	43.21 (0.25)	0.02 (0.02)	3.29 (0.05)	12.29 (0.19)	0.02 (0.02)	34.57 (0.23)	6.55 (0.11)	0.02 (0.02)	0.02 (0.01)	0.01 (0.01)	n.a.	b.d.l. ^a	0.31 (0.04)	*
S40F6	40.41 (0.21)	0.01 (0.01)	2.07 (0.04)	6.41 (0.08)	0.01 (0.01)	47.78 (0.23)	3.27 (0.08)	0.02 (0.01)	0.01 (0.01)	0.01 (0.01)	n.a.	b.d.l. ^a	0.32 (0.04)	*
S45F7	45.44 (0.18)	0.01 (0.01)	2.15 (0.05)	6.67 (0.11)	0.01 (0.01)	42.67 (0.19)	3.00 (0.08)	0.01 (0.01)	0.02 (0.01)	0.01 (0.01)	n.a.	b.d.l. ^a	0.34 (0.04)	*
S34F0	33.71 (0.17)	0.01 (0.01)	2.03 (0.04)	0.05 (0.02)	b.d.l.	48.98 (0.16)	15.19 (0.16)	0.01 (0.01)	b.d.l.	0.01 (0.01)	n.a.	b.d.l. ^a	-	*
S38F5W1	37.72 (0.14)	0.13 (0.02)	1.59 (0.03)	5.37 (0.06)	0.11 (0.02)	51.44 (0.13)	2.73 (0.06)	0.17 (0.02)	0.02 (0.01)	n.a.	0.07 (0.01)	0.65 (0.06)	n.a.	1,2,*
S40F5W6	37.34 (0.21)	0.13 (0.02)	1.84 (0.06)	4.32 (0.09)	0.09 (0.01)	47.91 (0.22)	2.58 (0.07)	0.18 (0.03)	0.03 (0.01)	n.a.	0.07 (0.01)	5.51 (0.52)	n.a.	1,2,*
S43F7W8	39.10 (0.20)	0.20 (0.03)	2.28 (0.04)	6.13 (0.08)	0.12 (0.02)	39.87 (0.20)	3.82 (0.06)	0.23 (0.02)	0.03 (0.01)	n.a.	0.08 (0.01)	8.13 (0.77)	n.a.	1,2,*
S39F6W12	33.75 (0.19)	0.08 (0.02)	1.39 (0.04)	4.86 (0.07)	0.06 (0.02)	46.38 (0.14)	1.68 (0.08)	0.12 (0.02)	0.01 (0.01)	n.a.	0.06 (0.01)	11.62 (1.10)	n.a.	1,2,*
S42F7	41.54 (0.63)	0.12 (0.02)	2.60 (0.04)	6.53 (0.23)	n.a.	42.68 (0.67)	6.18 (0.16)	0.28 (0.02)	n.a.	n.a.	0.13 (0.02)	n.a.	n.a.	³

218 ^a no signal was detected in the near-infrared region around 3530 cm⁻¹, which corresponds to the asymmetrical broad band due to
 219 the fundamental O-H stretching vibrations in OH groups and H₂O molecules. It indicates that the glasses produced by ADL are
 220 essentially dry.

221

222 2.3. Mössbauer analyses

223 Glass pieces of roughly 2 mm diameter were embedded in epoxy that was cut into disks
 224 with thicknesses between 400 and 500 μm, which is close to the optimum thickness for these
 225 compositions. Mössbauer spectra were recorded at room temperature (293 K) in transmission
 226 mode on a constant acceleration Mössbauer spectrometer with a nominal 370 MBq ⁵⁷Co high

227 specific activity (point) source in a 12 μm thick Rh matrix. The velocity scale was calibrated
228 relative to 25 μm thick $\alpha\text{-Fe}$ foil and spectra were collected over the range $\pm 5 \text{ mm s}^{-1}$ for 1 to 3
229 days each. Spectra were fitted with the full transmission integral using MossA software (Prescher
230 et al., 2012). Values of $\text{Fe}^{3+}/\text{Fe}_{\text{tot}}$ were calculated from relative areas and are listed in Tab. 1.

231

232 *2.4. Raman spectroscopy*

233 The as-prepared peridotite glasses were characterized by Raman spectroscopy on optically
234 polished surfaces using a Renishaw Invia Reflex Raman spectrometer equipped with a 514 nm
235 green laser (50 mW nominal power, operated at 10%) and a 1800 mm^{-1} grating. Spectra were
236 acquired with a 100x objective in the ranges 200–1500 cm^{-1} and 2700–4000 cm^{-1} , with 30 s
237 acquisition time and 2 accumulations. The samples subjected to DSC and micropenetration were
238 also characterized before and after the measurements using a confocal Raman imaging microscope
239 (alpha300R, WITec GmbH) at the Institute of Non-Metallic Materials, Clausthal University of
240 Technology (Germany). The Raman microscope is equipped with a 100x objective, a 532 nm diode
241 green laser and a CCD detector. The integration time employed with the alpha300R microscope
242 was 7 s (3 accumulations, 13 mW laser power). Raman spectra were invariably collected on
243 polished or cleanly broken surfaces, to exclude possible surface effects. Spectra were acquired in
244 the range from 200 to 1300 cm^{-1} . The Raman spectrometer was calibrated using a silicon standard.

245

246 *2.5. Calorimetry*

247 We subjected $\sim 20 \pm 5 \text{ mg}$ of glass to controlled heat treatments in a conventional
248 differential scanning calorimeter at the Institute of Non-Metallic Materials, Clausthal University
249 of Technology (CDSC, 404 C, Netzsch) using PtRh20 crucibles and under $\text{N}_2 5.0$ ($\geq 99.999\%$)

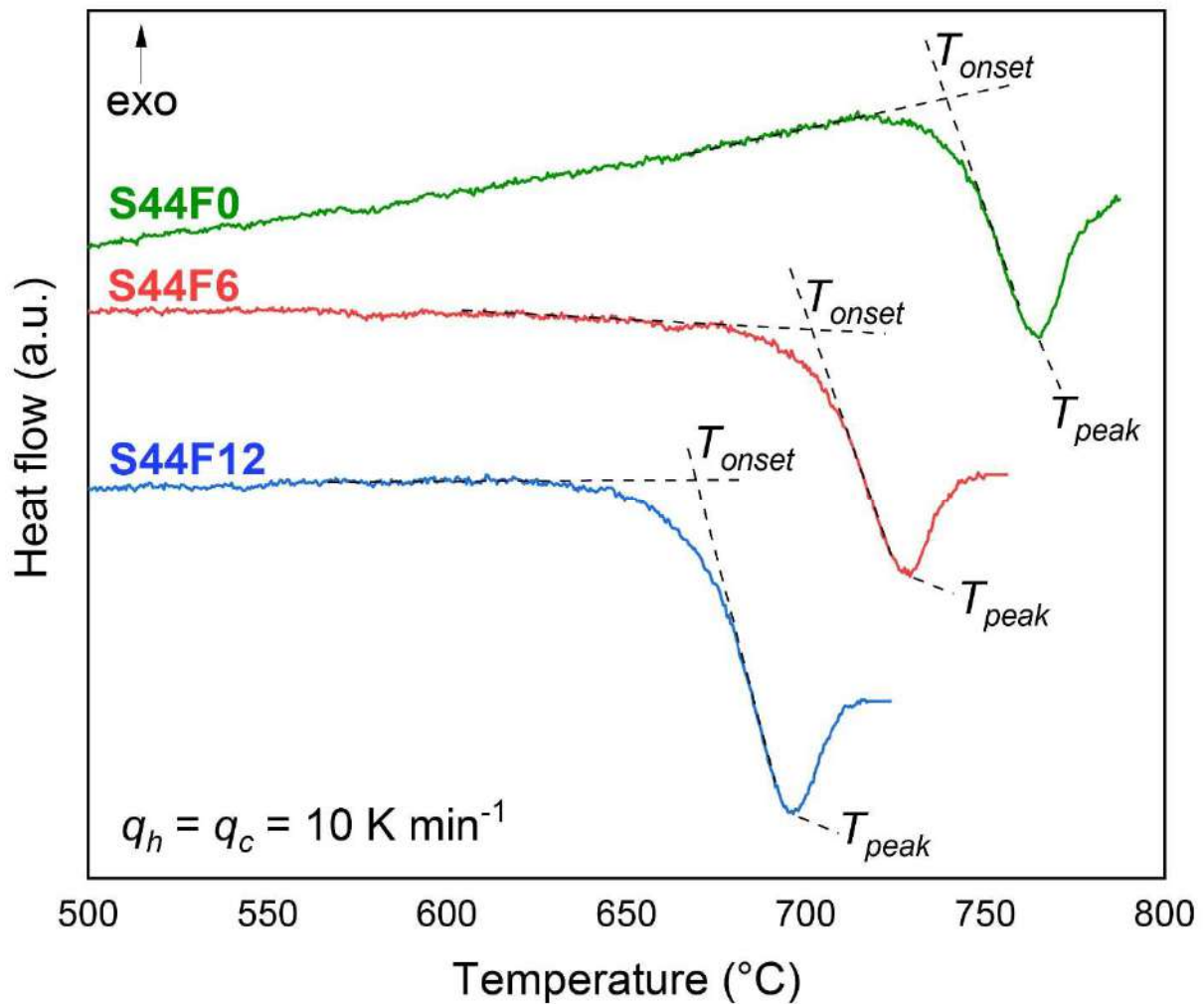
250 purity) atmosphere. Moreover, we used a few ng for flash calorimetry measurements (FDSC,
251 Mettler Toledo Flash DSC 2+ equipped with a UFH 1 sensor), under constant gas flow (40 ml min⁻¹
252 ¹) of Ar 5.0. The CDSC was calibrated using melting temperatures and enthalpy of fusion of
253 reference materials (pure metals: In, Sn, Bi, Zn, Al, Ag, and Au) up to 1337 K. The FDSC was
254 calibrated using the melting temperature of aluminium (melting temperature 933.6 K) and indium
255 (melting temperature 429.8 K).

256 We employed the matching rates methodology (Stabile et al., 2021) to measure the
257 characteristic temperatures T_{onset} and T_{peak} (Fig. 1). For the CDSC, we first allowed sample
258 relaxation by heating the starting material at 20 K min⁻¹ from room temperature to the glass
259 transition interval. Afterwards, the sample was cooled at a q_c of either 10 or 20 K min⁻¹ down to
260 373 K and subsequently heated at $q_h \equiv q_c$ (i.e, matching rates). For the FDSC, we used the same
261 procedure but at higher q_h (from 6,000 to 1,800,000 K min⁻¹, namely from 100 to 30,000 K s⁻¹)
262 listed in Tab. 3. T_{onset} represents the onset of the glass transition interval: it corresponds to the
263 intersection of two tangents, the first applied to the calorimetric trace pertaining to the glass and
264 the second at the inflection point during the glass transition, this latter identified as zero point on
265 the first derivative of the signal. It should be noted that T_{onset} can be more precisely identified using
266 a recently described method (Mancini et al., 2021), which however requires a 4-fold repetition of
267 the measurement (impractical for samples of small size and strong crystallization tendency) and a
268 smoothing of the average curve. On the other hand, T_{peak} , which is identified as the minimum on
269 the second derivative of the signal, represents the signal undershoot of the matching upscan in
270 Figure 1 (Al-Mukadam et al., 2021b, 2020; Di Genova et al., 2020b).

271 Further details about the fast heating and cooling of the FDSC, especially the differences
272 with respect to the CDSD, are described in previous studies and patents (Vanden Poel et al., 2012,

273 2011). In short, the FDSC chip sensor has four thermocouples in total, which guarantee high
274 sensitivity and high temperature resolution. The temperature resolution is enhanced by a lower
275 time constant of the sensor, which is ~ 0.2 ms in the FDSC, that is approximately $\sim 10,000$ times
276 less than that of a CDSC instrument.

277



278

279 *Figure 1. Measured heat flow using a conventional DSC as a function of temperature for samples*
280 *S44F0, S44F6 and S44F12 at a heating rate of 10 K min^{-1} , following a cooling rate of 10 K min^{-1}*
281 *through the glass transition interval. The characteristic glass transition temperatures (T_{onset} and*
282 *T_{peak}) are shown in the figure. a.u. – arbitrary units.*

283

284 *2.6. Micropenetration viscometry*

285 We subjected polished plane-parallel glass chips (2-2.5 mm thick) to micropenetration viscometry
286 measurements. We used a vertical dilatometer (Bähr VIS 404) at the Institute of Non-Metallic
287 Materials, Clausthal University of Technology. The setup consists of a SiO₂ rod pushing a sapphire
288 sphere of radius $r = 0.75$ mm, under a constant Ar flow, using a force of 3.92 N (400 g load). The
289 temperature was controlled with an S-type thermocouple (Pt-PtRh) placed at ~2 mm from the
290 sample surface. The temperature error is estimated at ± 5 K considering the accuracy of the S-type
291 thermocouple and its distance from the sample (Behrens et al., 2018). We followed standard
292 procedures (Di Genova et al., 2014a) to achieve thermal equilibration of the sample at the target
293 measuring temperature: a heating rate of 10 K min⁻¹ was used up to a temperature 100 K lower
294 than the target temperature, which was then approached with a slower heating rate of 5 K min⁻¹.
295 After reaching the final dwell temperature, the samples were allowed to relax before the load was
296 applied. The indentation depth of the sapphire sphere into the sample was measured as a function
297 of time using a linear variable displacement transducer and viscosity was determined according to
298 the literature (Douglas et al., 1965). Viscosity measurements of the standard glass DGG-1 were
299 used to calibrate the vertical dilatometer. The certified viscosity data (Meerlender, 1974) were
300 reproduced with a standard deviation of ± 0.1 in log units.

301

302 *2.7. Brillouin spectroscopy*

303 Prior to Brillouin scattering measurements, samples were double-polished to a thickness of
304 approximately 50 μm . The measurements were conducted using the system installed at BGI (Trots
305 et al., 2013), which includes a Coherent Verdi V2 solid-state Nd:YVO₄ laser with a 532 nm single
306 wavelength output and a six-pass Sandercock-type tandem Fabry-Perot interferometer equipped

307 with a Hamamatsu C11202-050 single-pixel photon-counting module. Focusing-collecting optics
308 with 100 mm focal lengths were employed to focus the laser beam on the sample position and to
309 collect the scattered inelastic signal. A laser power of 0.03 W was used in all measurements. The
310 measurements were performed in a forward platelet symmetric geometry with an angle of 80°
311 between the incident and scattered beams. This geometry allows the refractive index of the sample
312 to be neglected when calculating sound velocities from the frequency shifts of inelastically
313 scattered photons (Sinogeikin et al., 2006; Whitfield et al., 1976). Measurements were repeated 4
314 to 8 times at different azimuthal angles to account for possible platelet tilt or polishing
315 imperfection. As the acoustic wave velocities in isotropic solids are independent on sample
316 orientation, results at different angles were averaged. Experimentally determined Brillouin
317 frequency shifts $\Delta\omega$ were converted to longitudinal v_p and shear v_s sound velocities according to
318 the equation (Eq. 8):

319

$$320 \quad v = \frac{\Delta\omega\lambda}{2\sin(\theta/2)} \quad (8)$$

321

322 where λ is the laser wavelength and θ is the angle between the incident and scattered beams
323 (Sinogeikin et al., 2006; Whitfield et al., 1976).

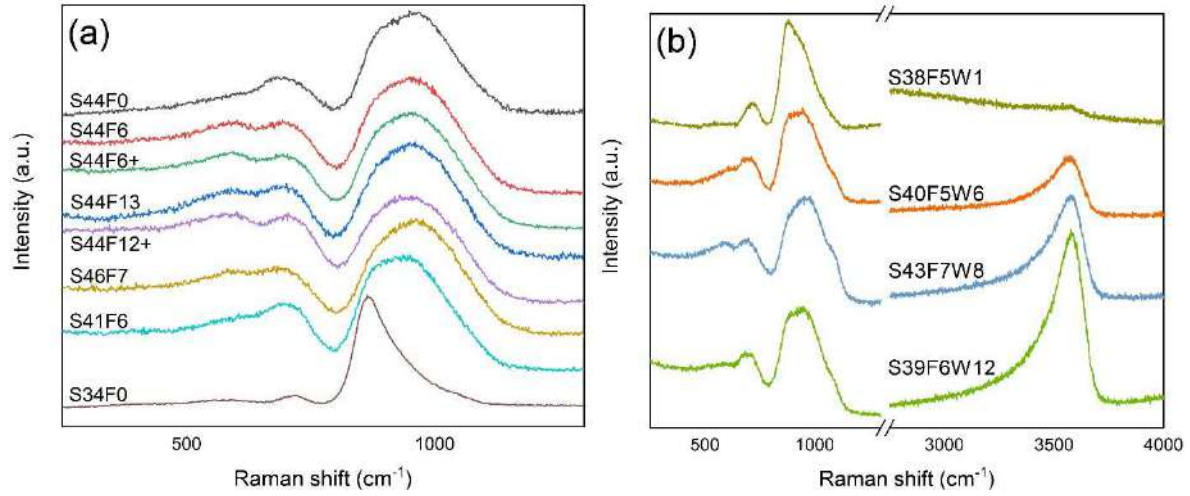
324

325 **3. Results**

326 *3.1 Overall characterization and vibrational spectroscopies*

327 Table 1 lists the chemical composition of the glasses (mol%) considered in this study,
328 determined by electron microprobe analysis; Fe³⁺/Fe_{tot} ratios were obtained by Mössbauer
329 spectroscopy. The amorphous nature of these hydrous and anhydrous peridotite glasses was

330 confirmed by Raman spectroscopy (Fig. 2): the obtained Raman spectra matched well with those
331 reported by previous authors for similar compositions (Bondar et al., 2022; Cooney and Sharma,
332 1990; Durben et al., 1993; Williams et al., 1989). In particular, we observed the general absence
333 of intense vibrational features at low wavenumber ($<600\text{ cm}^{-1}$) and the invariable occurrence of a
334 broad vibrational envelope in the range $800\text{--}1100\text{ cm}^{-1}$, following the substantial structural
335 depolymerization of these glasses as inferred by the theoretical number of non-bridging oxygens
336 per atom of a tetrahedrally coordinated cation $\text{NBO}/\text{T} \approx 2.9$ (Bondar et al., 2022). The substitution
337 of up to 12 mol% MgO by FeO (as in sample S44F12 compared to S44F0) and the different
338 $\text{Fe}^{3+}/\text{Fe}_{\text{tot}}$ ratios obtained by O_2 or Ar melting (as in S44F12 and S44F12+) did not seem to have
339 appreciable effects on the Raman spectra. Only S34F0 markedly differed from the other melt-
340 quenched glasses, most likely due to its much lower SiO_2 content: its spectrum is very similar to
341 that of pure forsterite glass (Williams et al., 1989). The observation of vibrational features at ~ 3600
342 cm^{-1} in hyperquenched high-pressure peridotite glasses confirmed the successful incorporation of
343 H_2O in their structure. As noticed previously (Bondar et al., 2022), the high-wavenumber envelope
344 of these hydrous glasses was shifted to higher wavenumbers as compared to their anhydrous
345 counterparts, which could suggest partial water-driven repolymerization (Xue and Kanzaki, 2004)
346 or a different $\text{Fe}^{3+}/\text{Fe}_{\text{tot}}$ ratio (Di Genova et al., 2016b).



347

348 *Figure 2. Raman spectra of peridotite glasses synthesized within this work. (a) Anhydrous*
 349 *peridotite glasses synthesized by ADL, dominated by an intense high-wavenumber envelope*
 350 *manifesting their extreme structural depolymerization. (b) Hydrated peridotite glasses synthesized*
 351 *using a novel rapid-quench multi-anvil technique, in which the incorporation of water is*
 352 *demonstrated by the appearance of intense Raman features at $\sim 3500 \text{ cm}^{-1}$.*

353

354 *Table 2. Measured acoustic wave velocities (v_s and v_p), calculated elastic moduli ratio (K/G , Eq.*
 355 *4), and melt fragility (m , Eq. 3) for all samples synthesized within this work. Numbers in parentheses*
 356 *provide the uncertainty of the last digit(s).*

357

Sample	v_s (m s ⁻¹)	v_p (m s ⁻¹)	K/G	m
S44F0	3826 (1)	6953 (5)	1.97 (1)	54.7 (1)
S44F6+	3757 (3)	6850 (5)	1.99 (1)	55.6 (2)
S44F6	3718 (3)	6825 (3)	2.04 (1)	57.6 (2)
S44F12+	3627 (3)	6695 (3)	2.07 (1)	59.2 (2)
S44F12	3636 (3)	6697 (3)	2.06 (1)	58.6 (2)
S41F6	3755 (7)	6917 (4)	2.06 (1)	58.6 (2)
S46F7	3736 (4)	6822 (1)	2.00 (1)	55.9 (2)
S34F0	3819 (9)	7016 (9)	2.04 (2)	57.8 (5)
S38F5W1	3774 (3)	6965 (4)	2.07 (1)	59.1 (2)
S40F5W6	3835 (5)	6989 (5)	1.99 (1)	55.5 (3)
S43F7W8	3768 (9)	6815 (16)	1.94 (2)	53.3 (6)
S39F6W12	3830 (4)	6899 (5)	1.91 (1)	52.1 (2)

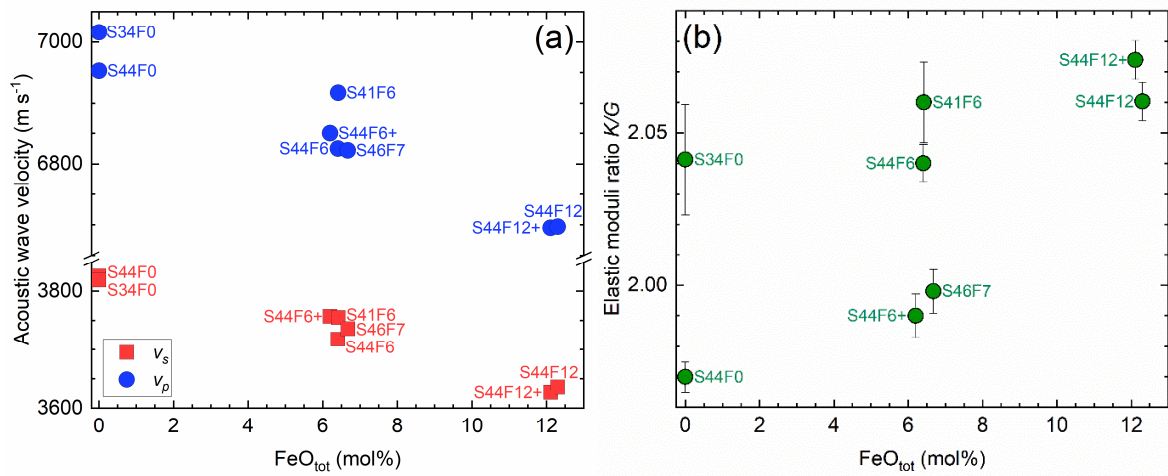
358

359

360 The measured shear v_s and longitudinal v_p acoustic wave velocities, the calculated elastic
 361 moduli ratio K/G and fragility index m are reported in Tab. 2. The iron content (FeO_{tot} in mol%)
 362 appeared to be the main compositional parameter controlling the acoustic wave velocities in the
 363 measured anhydrous samples (Fig. 3a). The iron-free S44F0 and S34F0 glasses exhibited the

364 highest recorded velocities, with v_s 3826(1) and 3819(9) m s⁻¹ and v_p 6953(5) and 7016(9) m s⁻¹,
 365 respectively. In contrast, the most Fe-rich samples S44F12 and S44F12+ showed the lowest v_s
 366 (respectively 3636(3) and 3627(3) m s⁻¹) and v_p values (respectively 6697(3) and 6695(3) m s⁻¹).
 367 Samples with an intermediate iron content plot in between.

368 The calculated K/G values (Eq. 4) exhibited a similar dependence on the FeO_{tot} content,
 369 superimposed on the influence of the overall SiO_2 content of the glasses, as expected from previous
 370 results (Cassetta et al., 2021). Within the S44F series (Fig. 3b), K/G ratios increased from 1.97(1)
 371 (S44F0) to 2.07(1) (S44F12+ and S44F12), with S44F6 and S44F6+ plotting at intermediate values
 372 (2.04(1) and 1.99(1), respectively). At similar FeO_{tot} contents (i.e., S44F0 and S34F0), SiO_2 -richer
 373 samples exhibited instead a substantially lower K/G .

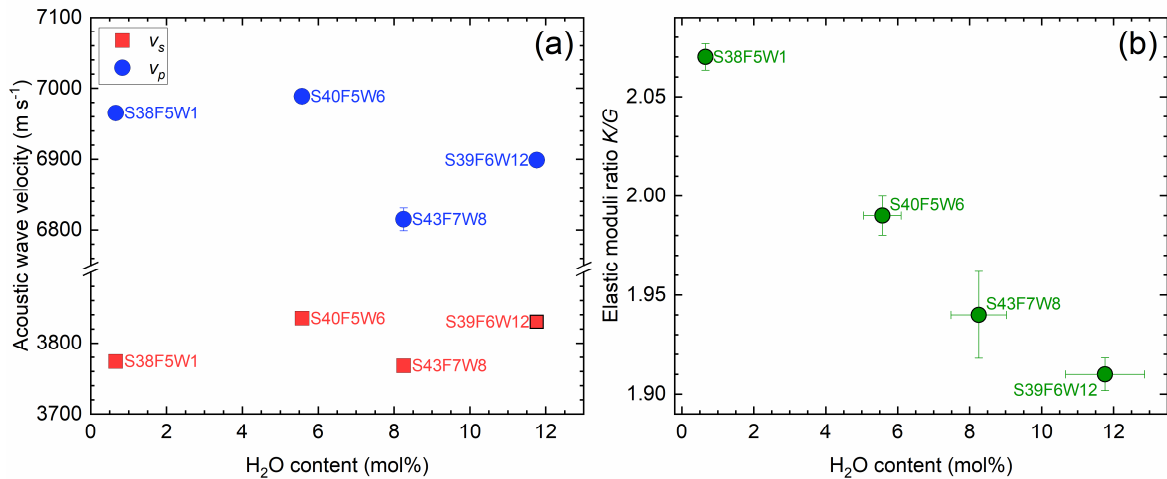


374

375 *Figure 3. Results of BLS measurements performed on anhydrous peridotite glasses, plotted as a*
 376 *function of their FeO_{tot} content (mol%). (a) Acoustic wave velocities generally decrease as FeO_{tot}*
 377 *increases, while (b) K/G ratios exhibit the opposite behaviour, superposed by a lesser dependence*
 378 *on the SiO_2 content of the glasses. Whenever absent, error bars are smaller than the depicted*
 379 *symbols.*

380

381 For the hydrous samples ($\text{FeO}_{\text{tot.}} = 5.2 \pm 1 \text{ mol\%}$), acoustic wave velocities v_s and v_p did
 382 not exhibit a clear dependence on water content (Fig. 4), which ranged between 0.65 (S38F5W1)
 383 and 11.62 mol% (S39F6W12). Nevertheless, the K/G ratio decreased proportionally to the degree
 384 of hydration, to the point that glass S39F6W12 showed the lowest recorded value in this study
 385 (1.91(1)) despite the very low overall SiO_2 content ($\sim 34 \text{ mol\%}$, i.e., $\sim 39 \text{ mol\%}$ of its anhydrous
 386 base composition). Although the measured K/G ratios locate slightly outside the range investigated
 387 previously (Cassetta et al., 2021), we converted K/G ratios into fragility m using Eq. 3: S39F6W12
 388 showed the lowest m (52.1(2)), whereas S44F12+ (anhydrous, highest $\text{FeO}_{\text{tot.}}$) exhibited the
 389 highest value (59.2(2)).



390
 391 *Figure 4. Results of BLS measurements performed on hydrous peridotite glasses, plotted as a*
 392 *function of their H₂O content. (a) Acoustic wave velocities do not show an appreciable trend, but*
 393 *(b) K/G ratios clearly decrease proportionally to the hydration degree of the glasses. Whenever*
 394 *absent, error bars are smaller than the depicted symbols.*

395

396 3.2 (Flash) calorimetry

397 Table 3 lists the measured characteristic temperatures T_{onset} and T_{peak} as a function of the
 398 heating rate: anhydrous samples could be characterized by CDSC ($q_h = 10$ and 20 K min^{-1}), while

399 the low available amounts and high instability of hydrous glasses made them suitable only for
400 FDSC ($q_h = 100$ and $30,000$ K min⁻¹). In agreement with the literature (Di Genova et al., 2014b),
401 the values of T_{onset} and T_{peak} increased with increasing q_h for both anhydrous and hydrous samples.

402 As observed for the sound velocities (Fig. 3), FeO_{tot} stood out as the major compositional
403 parameter controlling T_{onset} and T_{peak} in anhydrous samples, as they both decreased with increasing
404 iron content (Fig. 5). At $q_h = 10$ K min⁻¹, the highest T_{onset} and T_{peak} were obtained from S34F0
405 sample (1029 ± 3 and 1051 ± 1 K, respectively), whereas S44F12 showed the lowest T_{onset} and
406 T_{peak} (942 ± 3 and 969 ± 1 K, respectively). In samples with the same molar content of FeO_{tot} (e.g.,
407 S34F0 and S44F0), SiO₂ depletion seemed to lead to an increase in T_{onset} and T_{peak} . In line with the
408 literature (e.g., Bouhifd et al., 2004; Chevrel et al., 2013; Cukierman and Uhlmann, 1974; Di
409 Genova et al., 2017c), we measured (Tab. 3) a systematic effect of iron oxidation (Tab. 1) on the
410 DSC results: samples with a higher Fe³⁺/Fe_{tot} (S44F6+ and S44F12+) exhibited slightly higher
411 T_{onset} and T_{peak} than the reduced counterparts (S44F6 and S44F12).

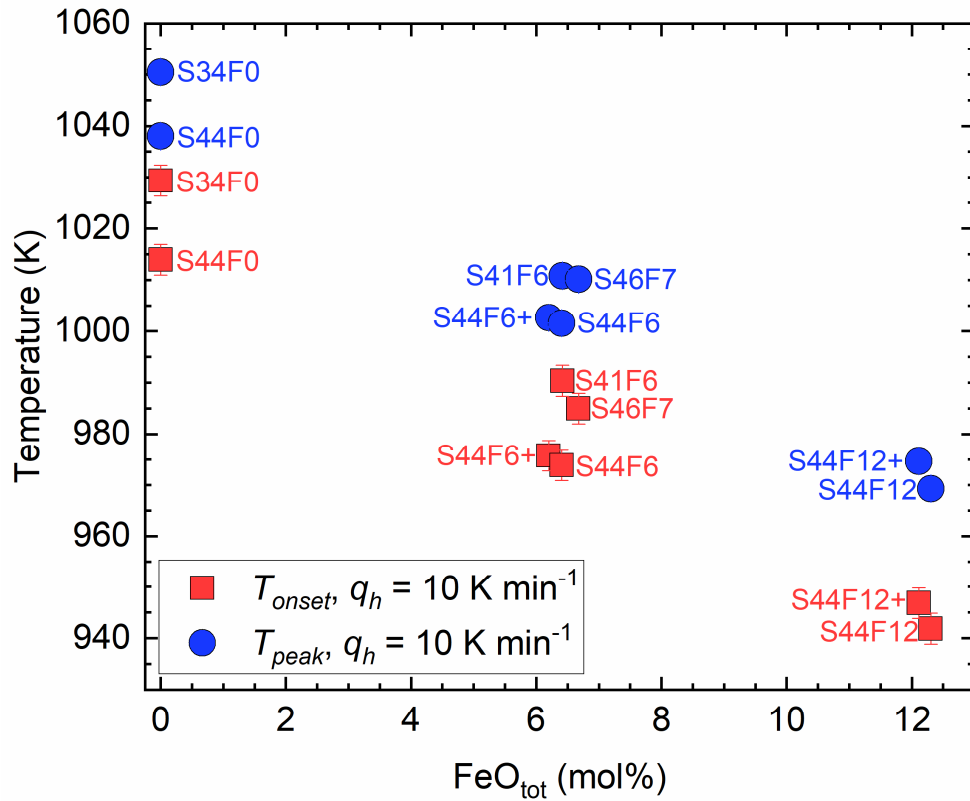
412

413 Table 3. Results of calorimetric measurements performed on peridotite glasses, from this work
414 and a literature reference (Dingwell et al., 2004). Viscosities associated with T_{onset} and T_{peak} for
415 all samples were calculated using Eq. 3 and shift factors (K_{onset} and K_{peak}) used in this study.
416 Temperature uncertainty (± 1 K for T_{peak} , ± 3 K for T_{onset}) was estimated based on repeated
417 measurements (only one for each sample and heating rate is reported here for brevity) and
418 calibration. Uncertainties for viscosity were estimated in a previous work (Di Genova et al.,
419 2020b), i.e. ± 0.15 for T_{onset} and ± 0.20 for T_{peak} . References: *this study, and ¹ (Dingwell et al.,
420 2004).

Method	Sample	q (K min ⁻¹)	q (K s ⁻¹)	T_{onset} (K)	$\log_{10} \eta$ (η in Pa s)	T_{peak} (K)	$\log_{10} \eta$ (η in Pa s)	Ref.	
CDSC	S44F0	10	0.17	1,014	11.98	1,038	10.62	*	
		20	0.33	1,019	11.68	1,046	10.32		
	S44F6+	10	0.17	976	11.98	1,003	10.62	*	
		20	0.33	983	11.68	1,010	10.32		
	S44F6	10	0.17	974	11.98	1,002	10.62	*	
		20	0.33	982	11.68	1,009	10.32		
	S44F12+	10	0.17	947	11.98	975	10.62	*	
		20	0.33	956	11.68	984	10.32		
	S44F12	10	0.17	942	11.98	969	10.62	*	
		20	0.33	950	11.68	977	10.32		
	S41F6	10	0.17	990	11.98	1,011	10.62	*	
	S46F7	10	0.17	985	11.98	1,010	10.62	*	
	S34F0	10	0.17	1,029	11.98	1,050	10.62	*	
	S42F7	5	0.08				1,006	10.92	
		8	0.13				1,013	10.72	
		10	0.17				1,013	10.62	1
15		0.25				1,017	10.44		
20		0.33				1,018	10.32		
FDSC	S38F5W1	6,000	100	1,025	9.20	1,066	7.84		
		12,000	200	1,036	8.90	1,072	7.54		
		18,000	300	1,041	8.72	1,075	7.36		
		30,000	500	1,045	8.50	1,080	7.14		
		60,000	1,000	1,055	8.20	1,090	6.84		
		180,000	3,000	1,069	7.72	1,109	6.36	*	
		300,000	5,000	1,074	7.50				
		420,000	7,000	1,077	7.35				
		600,000	10,000	1,084	7.20				
		1,200,000	20,000	1,095	6.90				
	1,800,000	30,000	1,098	6.72					
	S40F5W6	60,000	1,000	938	8.20	1,007	6.84	*	
S43F7W8	60,000	1,000	896	8.20	960	6.84	*		
S39F6W12	60,000	1,000	879	8.20			*		

421

422



423

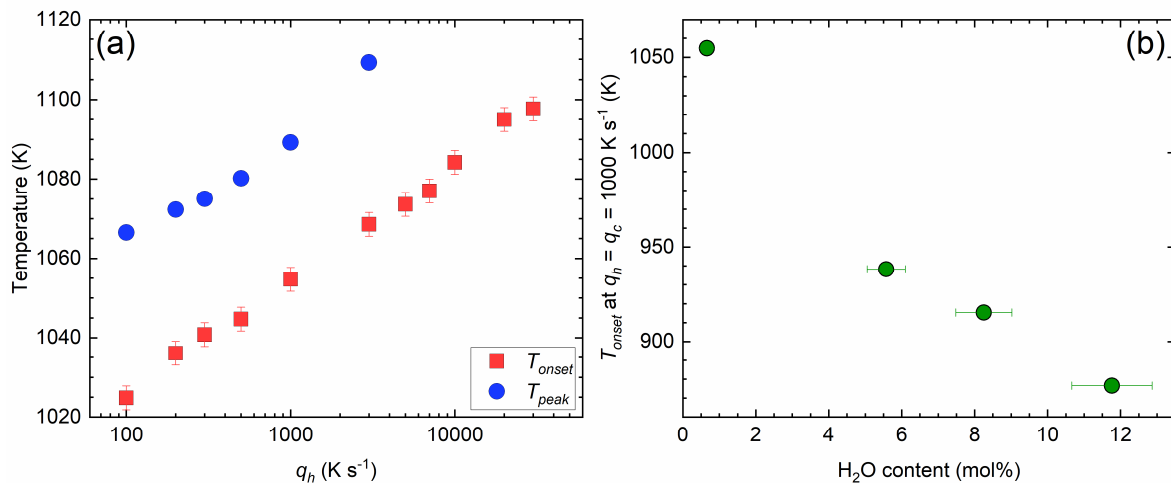
424 *Figure 5. Characteristic temperatures T_{onset} and T_{peak} of anhydrous peridotite glasses obtained*
 425 *from conventional DSC measurements performed at 10 K min^{-1} , plotted as a function of their*
 426 *FeO_{tot} content. T_{onset} and T_{peak} exhibit an overall reduction as the FeO_{tot} content of the glasses*
 427 *increases. Whenever absent, error bars are smaller than the depicted symbols.*

428

429 Due to the instability of hydrous peridotite glasses, we used the most H_2O -poor sample
 430 (S38F5W1) to successfully test the reproducibility of our FDSC approach, performing
 431 measurements of T_{onset} and T_{peak} at the standard rate $q_h = 1000 \text{ K s}^{-1}$ before and after any other
 432 calorimetric run at a different heating rate (Fig. 6a, Fig. S1 and Tab. 3). Comparison of the values
 433 obtained at $q_h = 1000 \text{ K s}^{-1}$ revealed any sample modification through a shift in the values of T_{onset}
 434 and T_{peak} ; when such deviations were observed, Raman spectra were acquired to document that the
 435 sample changed during the measurement (i.e., crystallization and/or degassing). We indeed

436 demonstrated in several recent works that Raman spectroscopy can reveal the precipitation of
 437 nanosized Fe-Ti-oxides (as expected during calorimetric measurements of magmatic melts at deep
 438 undercooling, where transition metals are poorly soluble and homogeneous crystal nucleation
 439 prevails over crystal growth), with sensitivity extending even to the early stages of amorphous
 440 phase separation anticipating the occurrence of actual crystals (Di Genova et al., 2020b, 2020a,
 441 2017a, 2017b; Scarani et al., 2022; Zandona et al., 2022, 2021, 2019). Using this approach, we
 442 concluded that sample S38F5W1 may be reliably measured for q_h ranging between 100 and 30000
 443 K s^{-1} (see the expected linear dependence on q_h in Figure 6); we obtained $T_{onset} = 1055 \pm 3 \text{ K}$ and
 444 $T_{peak} = 1090 \pm 1 \text{ K}$ at $q_h = 1000 \text{ K s}^{-1}$. For $q_h \geq 5,000 \text{ K s}^{-1}$ we limited the matching upscans to
 445 temperatures $\leq T_{peak}$, as the exposure of the melt to higher temperatures induced partial
 446 crystallization (Di Genova et al., 2020b; Scarani et al., 2022), inferred from the opacification of
 447 the glass and the appearance of the sharp characteristic features (e.g., at $\sim 670 \text{ cm}^{-1}$) of Fe-Ti-oxide
 448 crystals in its Raman spectrum (Di Genova et al., 2020a, 2020b, 2017b).

449



450
 451 *Figure 6. Results of flash DSC measurements performed on hydrous peridotite glasses. (a) T_{onset}*
 452 *and T_{peak} obtained from sample S38F5W1, plotted as a function of the applied heating rate q_h . The*
 453 *linear trend confirms the absence of sample modification (e.g. crystallization and degassing)*

454 during the measurements. (b) T_{onset} values obtained at 1000 K min^{-1} from all hydrous peridotite
 455 glasses, plotted as a function of the water molar content: the higher the water content, the lower
 456 T_{onset} . Whenever absent, error bars are smaller than the depicted symbols.

457
 458 For samples with increasing water content (from 5.51 to 11.62 mol%), however, we
 459 collected T_{onset} and T_{peak} only at $q_h = 1000 \text{ K s}^{-1}$ (Fig. S2 and Tab. 3), since slower rates resulted in
 460 a low DSC signal and faster ones triggered crystallization and/or degassing due to the high-
 461 temperature exposure above T_f . No T_{peak} value could be acquired from sample S39F6W12, whose
 462 very high water content (11.62 mol%) led to instability that forced us to restrict the matching
 463 upscan to T_{onset} , thereby avoiding fast crystallization and/or degassing at higher temperatures.

464 The T_{onset} at $q_h = 1000 \text{ K s}^{-1}$ significantly decreased with increasing water content (Fig. 6b):
 465 we measured 1055, 938, 896 and $879 \pm 3 \text{ K}$ for samples S38F5W1, S40F5W6, S43F7W8 and
 466 S39F6W12, respectively.

467

468 3.3 Micropenetration viscometry

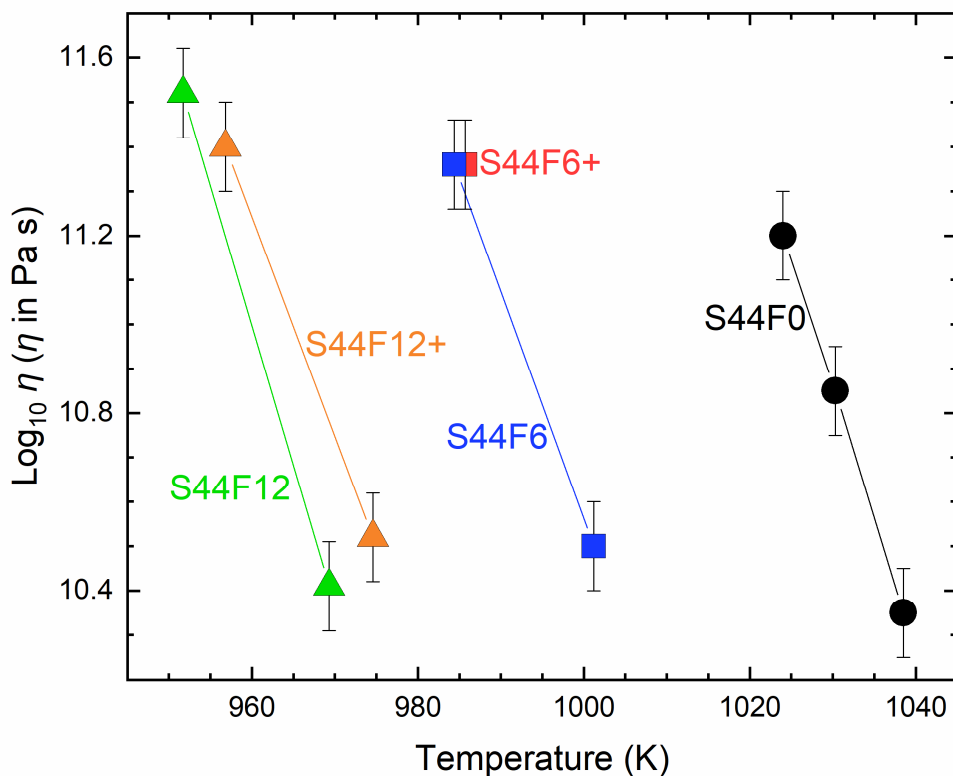
469 Table 4. Results of micropenetration viscometry measurements performed on some anhydrous
 470 peridotite glasses. Uncertainty is ± 0.1 in log unit based on calibration using DGG-1 standard
 471 glass (Meerlender, 1974).

472

Sample	Temperature (K)	$\log_{10} \eta$ (η in Pa s)
S44F0	1024	11.20
	1039	10.35
	1030	10.85
S44F6+	986	11.36
S44F6	984	11.36
	1001	10.50
S44F12+	957	11.40
	975	10.52
S44F12	952	11.52
	969	10.41

473

474 Table 4 lists the results of micropenetration viscometry that are plotted in Figure 7 as a
475 function of the temperature. We explored the effect of temperature, iron content, and iron oxidation
476 state on the melt viscosity using samples of the series S44F, characterized by the same SiO₂ content
477 (~44 mol%) but different FeO_{tot.} and Fe³⁺/Fe_{tot.}. As expected, the viscosity decreased with
478 increasing temperature for all samples. An increasing FeO_{tot.} (from 0 to 12 mol%) led to a
479 significant viscosity reduction: the iron-free sample (S44F0) had the highest recorded viscosity
480 (10^{10.35} Pa s at 1039 K), while the sample with the highest FeO_{tot.} (S44F12) exhibited a similar
481 viscosity (10^{10.41} Pa s) at a far lower temperature (969 K). Finally, we observed a minor effect of
482 the iron oxidation state, namely reduced samples (S44F6 and S44F12) were systematically less
483 viscous than oxidized samples (S44F6+ and S44F12+). For instance, S44F12 showed a viscosity
484 of 10^{10.41} Pa s at 969 K (Fe³⁺/Fe_{tot} = 0.31), whereas S44F12+ (Fe³⁺/Fe_{tot} = 0.50) exhibited a slightly
485 higher viscosity (10^{10.52} Pa s) at a lower temperature (975 K).



486

487 *Figure 7. Results of micropenetration viscometry measurements performed on anhydrous*
 488 *peridotite glasses with different FeO_{tot} content and Fe^{3+}/Fe_{tot} ratio. A higher FeO_{tot} content leads*
 489 *to lower viscosity values; more oxidized samples exhibit slightly higher viscosity than their*
 490 *reduced counterparts.*

491

492 4. Discussion

493 4.1. Evaluation and comparison between existing viscosity models

494 We used measured (Tab. 4) and DSC-derived (Tab. 3) viscosity data obtained from our
 495 twelve anhydrous and hydrous peridotite glasses to test the performance of existing viscosity
 496 models. We calculated the melt viscosity of our anhydrous and hydrous samples using the
 497 measured chemical composition (Tab. 1). The Hui and Zhang (2007) model (HZ) is based on the
 498 empirical equation (Eq. 9):

499

$$\log_{10} \eta = A + \frac{B}{T} + \exp\left(C + \frac{D}{T}\right) \quad (\text{Eq. 9})$$

501

502 where T is the temperature and the A , B , C and D parameters are computed based on the melt
503 composition. The Giordano–Russell–Dingwell model (GRD, Giordano et al., 2008) similarly
504 employs composition to estimate B and C parameters of the VFTH equation (Eq. 10):

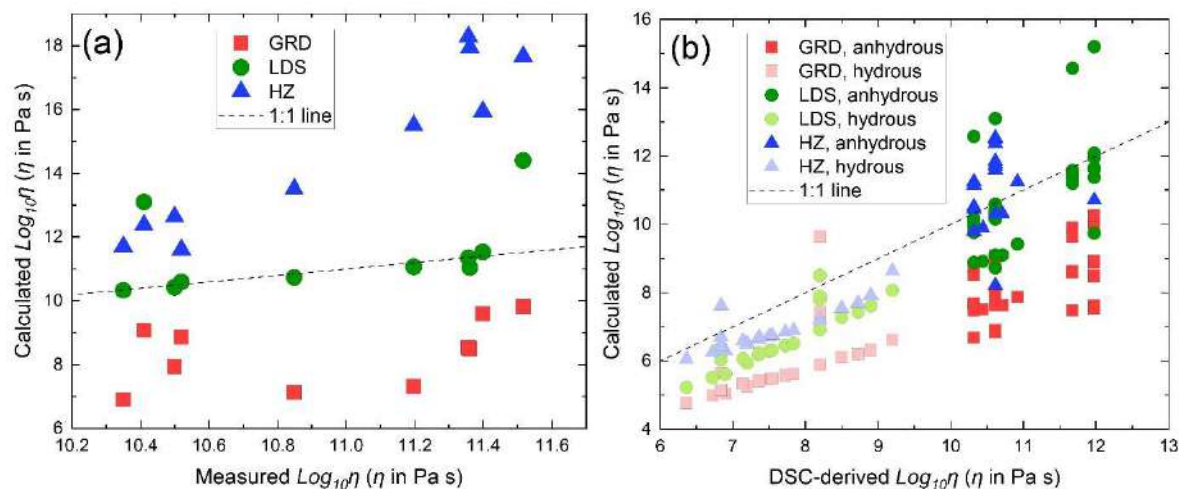
505

$$\log_{10} \eta = A + \frac{B}{T-C} \quad (\text{Eq. 10})$$

507

508 in which the viscosity at infinite temperature (A) is assumed constant ($10^{-4.55}$ Pa s) and iron is
509 treated as a single species (e.g., FeO_{tot}). The Langhammer–Di Genova–Steinle-Neumann model
510 (LDS, Langhammer et al., 2022) is based on artificial neural networks trained on the largest
511 viscosity database available for volcanic melts and also takes into account iron oxidation state; a
512 web application is available online at [https://domlang-visc-calc-final-script-](https://domlang-visc-calc-final-script-a1hbsg.streamlitapp.com/)
513 [a1hbsg.streamlitapp.com/](https://domlang-visc-calc-final-script-a1hbsg.streamlitapp.com/)

514 Figure 8a shows the comparison between our anhydrous micropenetration viscosity data
515 and model predictions (10 observations). Our measurements are severely underestimated or
516 overestimated by two of the selected models, respectively GRD and HZ. Conversely, the LDS
517 model predicts well the data except for those collected from S44F12, the sample with the highest
518 iron content and a comparatively low $\text{Fe}^{3+}/\text{Fe}_{\text{tot}}$ ratio. For a general evaluation of the quality of the
519 model predictions, we employed the root-mean-square error (RMSE) method and found that the
520 models by GRD and HZ achieve RMSE of 2.75 and 4.32 respectively, whereas LDS has a RMSE
521 of 1.25.



522

523 *Figure 8. Comparison between viscosity data determined within this work and numerical model*
 524 *predictions. (a) Viscosity measured by micropenetration on anhydrous peridotite melts and the*
 525 *respective prediction using viscosity models from literature; (b) viscosity data derived from (flash)*
 526 *DSC measurements and literature data (Dingwell et al., 2004) on anhydrous and hydrous*
 527 *peridotite melts and the respective prediction using viscosity models. Considered models: GRD*
 528 *(Giordano et al., 2008), LDS (Langhammer et al., 2022) and HZ (Hui and Zhang, 2007). Error*
 529 *bars on measured data have been omitted for clarity.*

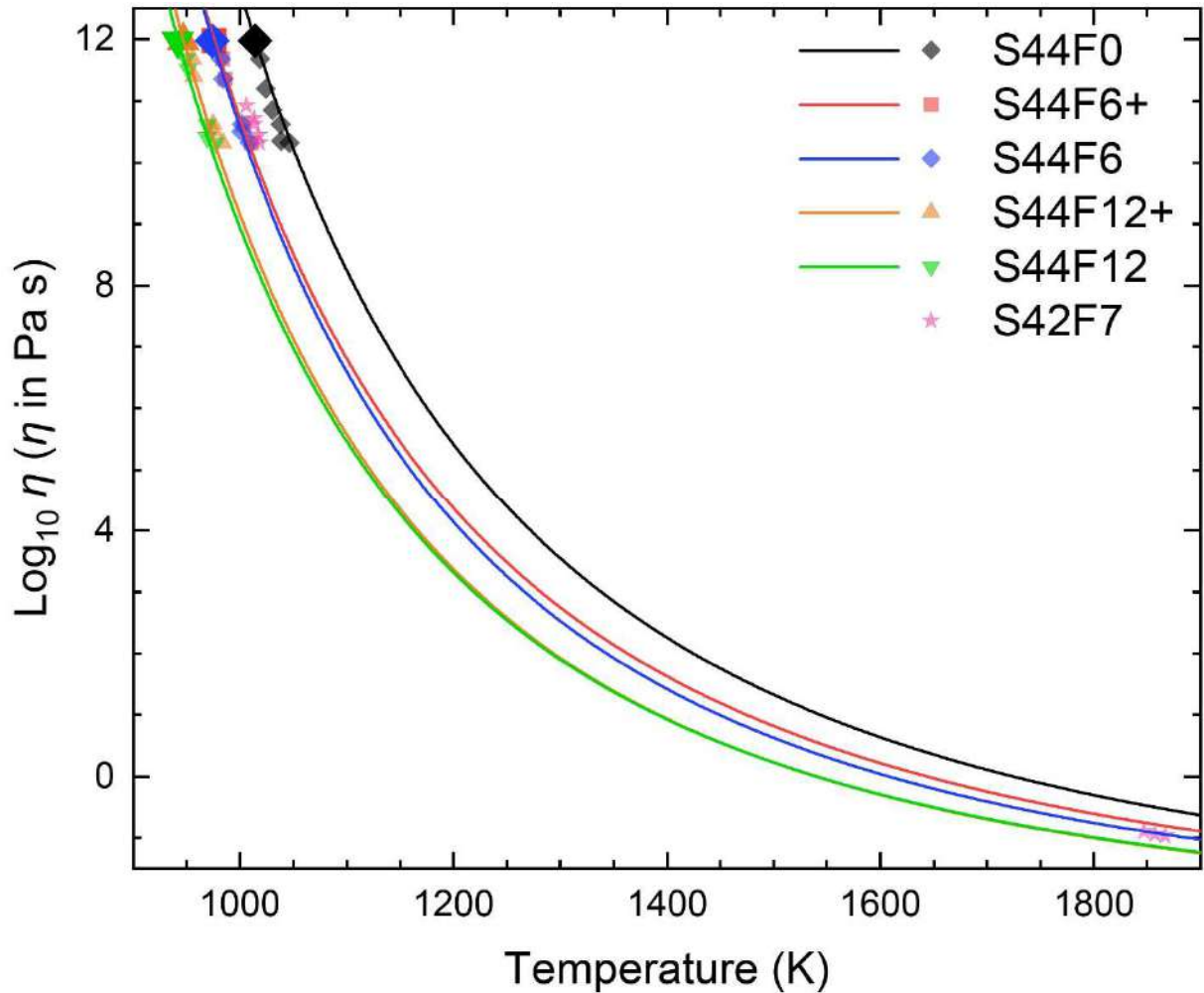
530

531 Figure 8b similarly illustrates the comparison between anhydrous and hydrous DSC-
 532 derived viscosity data (77 data points, of which 53 are reported in Tab. 3 while the rest corresponds
 533 to repetitions of FDSC measurements performed to ensure reproducibility, using the same heating
 534 rate and the same sample) and the predictions of the models. Our measurements are mainly
 535 underestimated by all models with the one by LDS performing best. The HZ model performs well
 536 overall, but predicts unrealistically high viscosities of $\sim 10^{20}$ Pa s for all T_{onset} at 10 and 20 K min⁻¹
 537 and $10^{34.74}$, $10^{18.75}$ and $10^{268.15}$ Pa s for the hydrous samples characterized by the highest water
 538 contents (5.51, 8.13 and 11.62 mol%, respectively). The predictions resulted in overall RMSE
 539 values of 1.21, 2.43 and 30.02 for LDS, GRD and HZ models, respectively.

540

541 4.2. Development of a viscosity model for peridotite melts

542 The experimental data gathered within this work enable a new tailored parameterization of
543 the viscosity of peridotite melts as a function of temperature and water content. Figure 9 shows
544 the modelled anhydrous viscosity (lines) for the S44F series using the MYEGA formulation (Eq.
545 1) the CDSC-derived T_g (i.e., T_{onset} at $q_h = 10 \text{ K min}^{-1}$ in Tab. 3) and the BLS-derived fragility
546 index m (Eq. 3 and Tab. 2). For comparison, we also plot viscosity data points measured within
547 this work (S44F series) and in the literature for S42F7 (Dingwell et al., 2004). Inspection of Figure
548 9 reveals that all experimental viscosity data points obtained by CDSC, micropenetration
549 viscometry, and high-temperature concentric-cylinder viscometry are accurately predicted by our
550 model, from T_g ($\eta = 10^{12} \text{ Pa s}$) down to $\eta \approx 10^{-1} \text{ Pa s}$ ($\sim 1850 \text{ K}$). This remarkable result confirms
551 that combining DSC and BLS (Cassetta et al., 2021) allows the reliable estimation of T_g and m
552 and, thereby, the prediction and modelling of melt viscosity without the strict need for viscosity
553 measurements; as evident, this approach can be reliably extended even to the exotic, highly
554 depolymerized peridotite melts investigated in this study. Moreover, $K_{onset} = 11.20 \pm 0.15$ and K_{peak}
555 $= 9.84 \pm 0.20$ are demonstrated to be chemically invariant for geological melts (Di Genova et al.,
556 2020b; Stabile et al., 2021). Overall, our modelling shows that the combined effect of changing
557 iron content and oxidation state ($\text{Fe}^{3+}/\text{Fe}_{\text{tot}}$) has a significant effect on melt viscosity, with the
558 largest effect at around T_g ($\eta = 10^{12} \text{ Pa s}$). For instance, at 1014 K the viscosity decreases by more
559 than three orders of magnitude from $\sim 10^{12} \text{ Pa s}$ for the iron-free sample (S44F0) to $\sim 10^{8.33} \text{ Pa s}$ for
560 the reduced sample with the highest FeO_{tot} (S44F12).



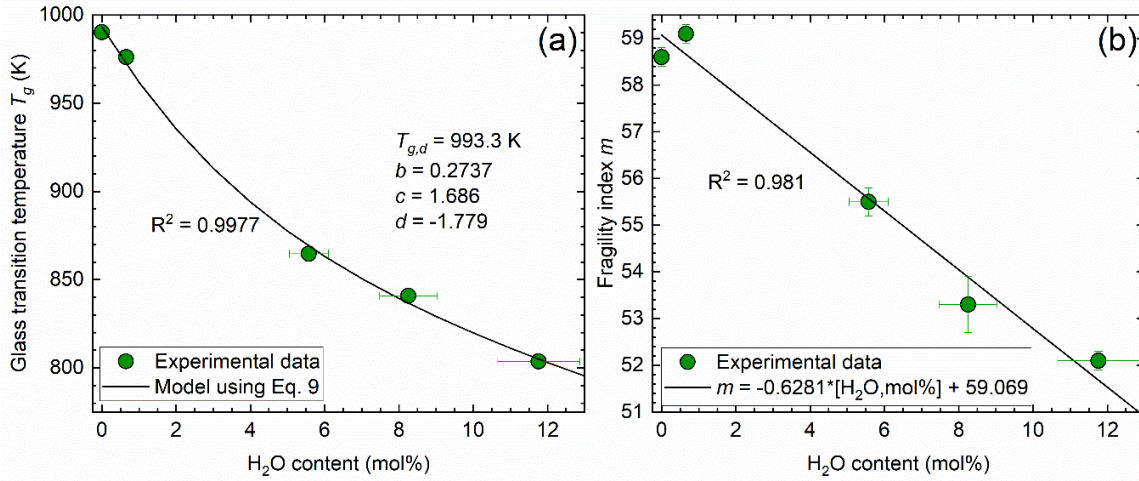
561

562 *Figure 9. MYEGA parameterization (Eq. 1) of the viscosity of anhydrous peridotite melts, based*
 563 *on DSC-derived T_g and BLS-computed fragility values m . A higher FeO_{tot} content perceivably*
 564 *lowers the viscosity of peridotite melts. Experimental viscosity data from this work and literature*
 565 *(pink stars, from Dingwell et al., 2004) are reported for comparison. Error bars are smaller than*
 566 *the depicted symbols.*

567

568 Modelling the viscosity of hydrous melts requires the knowledge of T_g as a function of
 569 water content. Direct T_g determination of hydrous samples could not be performed here because
 570 their size (in the order of ng) was suitable only for FDSC and not for CDSC measurements. For
 571 this reason, we obtained the values of T_g ($\eta = 10^{12}$ Pa s) of our hydrous samples by fitting the
 572 MYEGA equation (Eq. 1) to the FDSC-derived viscosity datapoints (η in the range $10^9 - 10^6$ Pa s,

573 as in Tab. 3), and by fixing fragility m to the value derived by BLS (Tab. 2). Figure 10 shows how
 574 the obtained T_g values decrease as expected with increasing water content: we found that T_g
 575 decreases by ~11% (from 976 to 865 K) from 0.7 to 5.5 mol% of water, while the reduction is by
 576 ~14% for H₂O = 8.1 mol% (T_g = 841 K) and ~18% for H₂O = 11.6 mol% (T_g = 804 K). Our
 577 findings are in line with T_g measurements of depolymerized melts such as foidite (NBO/T = 1.5)
 578 and tephrite (NBO/T = 0.9) from the literature (Bouhifd et al., 2013), where 5 mol% of water
 579 decreased T_g by a comparable amount.



580
 581 *Figure 10. Parameterization of (a) glass transition temperature T_g (model from Eq. 11,*
 582 *Langhammer et al. 2021) and (b) fragility index (m) of hydrous peridotite melts, as a function of*
 583 *their water content. Fit parameters and coefficient of determination R^2 are reported on each*
 584 *graph. Whenever absent, error bars are smaller than the depicted symbols.*

585
 586 Subsequently, we parameterized T_g as a function of the molar water content according to
 587 Eq. 11 (Langhammer et al., 2021):

588
 589
$$T_g(x_{H_2O}) = w_1 T_{g,H_2O} + w_2 T_{g,d} + c w_1 w_2 (T_{g,d} - T_{g,H_2O}) + d w_1 w_2^2 (T_{g,d} - T_{g,H_2O}) \quad (11)$$

590

591 with (Eq. 12)

592

$$593 \quad w_1 = \frac{x_{H_2O}}{b(100-x_{H_2O})+x_{H_2O}} \quad \text{and} \quad w_2 = \frac{b(100-x_{H_2O})}{b(100-x_{H_2O})+x_{H_2O}} \quad (12)$$

594

595 where X_{H_2O} is the mol% of dissolved water, $T_{g,d}$ is the glass transition temperature of the anhydrous

596 composition and T_{g,H_2O} is the glass transition temperature of pure water equal to 136 K (Kohl et

597 al., 2005). Note that b , c and d are fitting parameters. As for fragility indices, we linearly fit BLS-

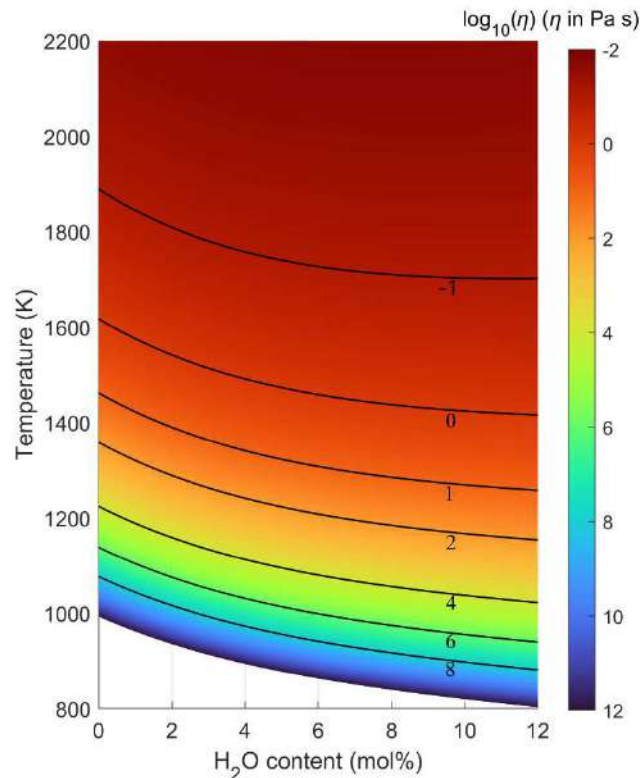
598 derived m (Eq. 3 and Tab. 2) as a function of water content. The results of these procedures are

599 summarized in Figure 11: the combination of the MYEGA equation (Eq. 1) with the description

600 of $T_g(H_2O)$ (Eq. 11) and $m(H_2O)$ (linear parameterization in Figure 10-b) enables the modelling of

601 the viscosity of hydrous peridotite melts as a function of temperature and dissolved water content.

602 We provide a viscosity calculator in the Supplementary Material.



603

604 Figure 11. Viscosity of hydrous peridotite melts as a function of temperature and H₂O content.
 605 Contour lines are labeled with the respective value of log η .

606

607 *4.3. Implications for Earth Science*

608 Highly ultramafic (peridotite) melts are expected to have formed during the magma ocean
 609 stage in the Earth's early history, and may be generated in the present-day deep mantle. Although
 610 data on supercooled peridotite liquids at ambient pressure presented in this study are not directly
 611 applicable to natural melts, they allow for a more robust extrapolation in the super-liquidus
 612 temperature range.

613 In the current deep mantle, highly ultramafic melts are produced by dehydration melting at
 614 the 660-km discontinuity due to the ringwoodite to bridgmanite + ferropericlase phase transitions
 615 (Schmandt et al., 2014). These melts are expected to be ultramafic and iron-enriched (Nakajima et
 616 al., 2019). The FeO_{tot} in the melts can reach 20 – 30 mol.% because of the high partitioning

617 coefficient of Fe/Mg between melt and solids, while the water content can reach about 20 – 50
618 wt.% (Fei, 2021; Ghosh and Schmidt, 2014; Nakajima et al., 2019). Although the pressure
619 conditions for the 660-km discontinuity (about 23 GPa) are much higher than the experimental
620 conditions in this study (ambient pressure), the pressure effect on melt viscosity is relatively small
621 (Xie et al., 2021, 2020). Thus, the viscosity of hydrous melt at high pressure is expected to be
622 lowered by more than two orders of magnitude compared to dry peridotite melt. Such a reduction
623 in melt viscosity may further enhance horizontal flow, leading to slab stagnation at the bottom of
624 the mantle transition zone as imaged seismologically (Fukao and Obayashi, 2013). On the other
625 hand, melt at the 660-km discontinuity is gravitationally unstable because of its low density
626 compared to the mantle transition zone (Fei, 2021; Nakajima et al., 2019). Its low viscosity may
627 enhance the upwelling of the melt, which returns water from the subducting slabs back to the
628 mantle transition zone.

629 In the early history of the Earth, the mantle is expected to have experienced a large degree
630 of melting during accretion and later, after the Moon-forming giant impact, potentially forming a
631 series of terrestrial magma oceans composed of peridotite melt (e.g., Nakajima and Stevenson,
632 2015). Our results are relevant to the solidification process in a hydrous magma ocean under a
633 dense steam atmosphere. With increasing solid fractions during the cooling of the magma ocean,
634 the crystallized solids and remaining melt could form a homogeneously-distributed mush-like
635 phase if the melt viscosity is relatively high. However, the water-induced reduction of melt
636 viscosity accelerates the segregation of melt from solid by gravity, promoting compositional
637 layering within the planet's interior. On the other hand, it is important to point out that even a
638 significant amount of water (e.g., 10 mol% at 2000 K) has very small effect on viscosity at
639 temperatures > 1800 K (Figure 11). In such case, the physical effects of degassing and/or melting

640 point depression may have greater importance on magma ocean dynamics than the absolute value
641 of viscosity.

642 Finally, our data shed some light on the effect of water on polymerization in extremely
643 depolymerized melts. While the dissolution of water in polymerized melts depolymerizes them
644 (e.g., Stolper, 1982; Zotov and Keppler, 1998), the depolymerizing effect of water decreases with
645 increasing depolymerization (e.g., Mysen, 2014; Mysen and Cody, 2005; Xue and Kanzaki, 2004
646 and references therein). As a result, there is an ongoing debate over whether the addition of water
647 to extremely depolymerized melt has no or little depolymerizing effect, or whether it can
648 polymerize the melt. A recent Raman study on these peridotite glasses indicated a shift of the high-
649 wavenumber envelope to higher wavenumbers with increasing water content, suggesting
650 polymerization (Bondar et al., 2022). However, a subsequent FTIR study demonstrated that the
651 proportions of (Mg,Ca)OH and (Si,Al)OH species remain constant over a wide range of water
652 contents, suggesting a negligible effect of water on polymerization (Bondar et al., 2023). The
653 present study favors the latter hypothesis since clear decreases in viscosity and glass transition
654 temperature with increasing water contents are observed for this set of peridotite glasses.

655

656 **5. Conclusions**

657 Overcoming their strong tendency towards crystallization and degassing, we measured the
658 viscosity of anhydrous and hydrous peridotite melts by conventional viscometry, conventional
659 calorimetry, and flash calorimetry. We demonstrate that a combination of these techniques with
660 Brillouin spectroscopy enables the reliable description of melt viscosity between at least 10^{12} and
661 10^{-1} Pa s. With $m > 50$, peridotites are among the most fragile natural melts; their viscosity exhibits
662 a clear dependence on FeO_{tot} , H_2O and, to a lesser extent, SiO_2 content and iron oxidation state.

663 The addition of dissolved water leads to a marked and parallel reduction of both T_g and m , which
664 can substantially affect flow behavior at high and intermediate viscosity. We compared our results
665 with predictions from empirical models of volcanic melt viscosity: among long-established and
666 more recent ones, the recently developed neural-network-based model (Langhammer et al., 2022)
667 performed best. We also provide a calculator to derive the viscosity of peridotite melts as a function
668 of temperature and dissolved water content.

669 **Acknowledgements**

670 Danilo Di Genova acknowledges the funding from the European Research Council (ERC) under
671 the European Union's Horizon 2020 research and innovation programme (NANOVOLC, ERC
672 Consolidator Grant – No. 101044772). Danilo Di Genova acknowledges the Deutsche
673 Forschungsgemeinschaft (DFG) project DI 2751/2-1. Alessio Zandonà acknowledges the DFG for
674 funding his research through the Walter Benjamin Program, project no. 448961237, ZA 1188/1-1
675 and ZA 1188/2-1; he is also grateful to Dr. Mathieu Allix for granting access to the containerless
676 melting facility available at CNRS CEMHTI in Orléans (France). Joachim Deubener
677 acknowledges the funding of DFG under grant number DE 598/33-1.

678

679 **References**

- 680 Al-Mukadam, R., Di Genova, D., Bornhöft, H., Deubener, J., 2020. High rate calorimetry
681 derived viscosity of oxide melts prone to crystallization. *J. Non. Cryst. Solids* 536.
682 Al-Mukadam, R., Götz, I.K., Stolpe, M., Deubener, J., 2021a. Viscosity of metallic glass-
683 forming liquids based on Zr by fast-scanning calorimetry. *Acta Mater.* 221, 117370.
684 <https://doi.org/10.1016/j.actamat.2021.117370>
685 Al-Mukadam, R., Zandonà, A., Deubener, J., 2021b. Kinetic fragility of pure TeO₂ glass. *J. Non.*
686 *Cryst. Solids* 554, 1–6. <https://doi.org/10.1016/j.jnoncrysol.2020.120595>
687 Angell, C.A., 1995. Formation of Glasses from Liquids and Biopolymers. *Science* (80-.). 267,
688 1924–1935. <https://doi.org/10.1126/science.267.5206.1924>
689 Armstrong, J.T., 1991. Quantitative Elemental Analysis of Individual Microparticles with
690 Electron Beam Instruments, in: Heinrich, K.F.J., Newbury, D.E. (Eds.), *Electron Probe*

691 Quantitation. Springer US, Boston, MA, pp. 261–315. <https://doi.org/10.1007/978-1-4899->
692 [2617-3_15](https://doi.org/10.1007/978-1-4899-2617-3_15)

693 Behrens, H., Bauer, U., Reinsch, S., Kiefer, P., Müller, R., Deubener, J., 2018. Structural
694 relaxation mechanisms in hydrous sodium borosilicate glasses. *J. Non. Cryst. Solids* 497,
695 30–39. <https://doi.org/10.1016/j.jnoncrysol.2018.05.025>

696 Bondar, D., 2023. Speciation of water and molar absorptivities of near-infrared OH- and H₂O
697 bands in hydrous peridotitic glasses quenched by a novel rapid-quench multi-anvil
698 technique. University of Bayreuth.

699 Bondar, D., Fei, H., Withers, A.C., Ishii, T., Chanyshv, A., Katsura, T., 2021. A simplified
700 rapid-quench multi-anvil technique. *Rev. Sci. Instrum.* 92.
701 <https://doi.org/10.1063/5.0062525>

702 Bondar, D., Fei, H., Withers, A.C., Katsura, T., 2020. A rapid-quench technique for multi-anvil
703 high-pressure-temperature experiments. *Rev. Sci. Instrum.* 91.
704 <https://doi.org/10.1063/5.0005936>

705 Bondar, D., Withers, A.C., Whittington, A.G., Fei, H., Katsura, T., 2023. Dissolution
706 mechanisms of water in depolymerized silicate (peridotitic) glasses based on infrared
707 spectroscopy. *Geochim. Cosmochim. Acta* 342, 45–61.
708 <https://doi.org/https://doi.org/10.1016/j.gca.2022.11.029>

709 Bondar, D., Zandona, A., Withers, A.C., Fei, H., Di Genova, D., Miyajima, N., Katsura, T.,
710 2022. Rapid-quenching of high-pressure depolymerized hydrous silicate (peridotitic)
711 glasses. *J. Non. Cryst. Solids* 578. <https://doi.org/10.1016/j.jnoncrysol.2021.121347>

712 Bouhifd, M.A., Richet, P., Besson, P., Roskosz, M., Ingrin, J., 2004. Redox state, microstructure
713 and viscosity of a partially crystallized basalt melt. *Earth Planet. Sci. Lett.* 218, 31–44.
714 [https://doi.org/10.1016/s0012-821x\(03\)00641-1](https://doi.org/10.1016/s0012-821x(03)00641-1)

715 Bouhifd, M.A., Whittington, A.G., Withers, A.C., Richet, P., 2013. Heat capacities of hydrous
716 silicate glasses and liquids. *Chem. Geol.* 346, 125–134.
717 <https://doi.org/10.1016/j.chemgeo.2012.10.026>

718 Cassetta, M., Di Genova, D., Zanatta, M., Ballaran, T.B., Kurnosov, A., Giarola, M., Mariotto,
719 G., 2021. Estimating the viscosity of volcanic melts from the vibrational properties of their
720 parental glasses. *Sci. Rep.* <https://doi.org/10.1038/s41598-021-92407-5>

721 Cassidy, M., Manga, M., Cashman, K. V., Bachmann, O., 2018. Controls on explosive-effusive
722 volcanic eruption styles. *Nat. Commun.* 9, 2839. [https://doi.org/10.1038/s41467-018-05293-](https://doi.org/10.1038/s41467-018-05293-3)
723 [3](https://doi.org/10.1038/s41467-018-05293-3)

724 Chevrel, M.O., Giordano, D., Potuzak, M., Courtial, P., Dingwell, D.B., 2013. Physical
725 properties of CaAl₂Si₂O₈-CaMgSi₂O₆-FeO-Fe₂O₃ melts: Analogues for extra-terrestrial
726 basalt. *Chem. Geol.* 346, 93–105. <https://doi.org/10.1016/j.chemgeo.2012.09.004>

727 Cooney, T.F., Sharma, S.K., 1990. Structure of glasses in the systems Mg₂SiO₄-Fe₂SiO₄,
728 Mn₂SiO₄-Fe₂SiO₄, Mg₂SiO₄-CaMgSiO₄, and Mn₂SiO₄-CaMnSiO₄. *J. Non. Cryst. Solids*
729 122, 10–32. [https://doi.org/https://doi.org/10.1016/0022-3093\(90\)90220-G](https://doi.org/https://doi.org/10.1016/0022-3093(90)90220-G)

730 Cukierman, M., Uhlmann, D.R., 1974. Effects of Iron Oxidation State on Viscosity, Lunar
731 Composition 15555. *J. Geophys. Res.* 79, 1594–1598.
732 <https://doi.org/10.1029/JB079i011p01594>

733 Di Genova, D., Brooker, R.A., Mader, H.M., Drewitt, J.W.E.E., Longo, A., Deubener, J.,
734 Neuville, D.R., Fanara, S., Shebanova, O., Anzellini, S., Arzilli, F., Bamber, E.C.E.C.E.C.,
735 Hennem, L., La Spina, G., Miyajima, N., Deubener, J., La Spina, G., 2020a. In situ
736 observation of nanolite growth in volcanic melt: A driving force for explosive eruptions.

737 Sci. Adv. 6. <https://doi.org/10.1126/sciadv.abb0413>

738 Di Genova, D., Cimarelli, C., Hess, K.-U., Dingwell, D.B., 2016a. An advanced rotational
739 rheometer system for extremely fluid liquids up to 1273 K and applications to alkali
740 carbonate melts. *Am. Mineral.* 101, 953–959. <https://doi.org/10.2138/am-2016-5537CCBYNCND>

741

742 Di Genova, D., Hess, K.-U., Chevrel, M.O., Dingwell, D.B., 2016b. Models for the estimation of
743 Fe³⁺/Fetot. ratio in terrestrial and extra-terrestrial alkali- and iron-rich silicate glasses
744 using Raman spectroscopy. *Am. Mineral.* 101, 943–952. <https://doi.org/10.2138/am-2016-5534CCBYNCND>

745

746 Di Genova, D., Kolzenburg, S., Wiesmaier, S., Dallanave, E., Neuville, D.R., Hess, K.-U.,
747 Dingwell, D.B., 2017a. A chemical tipping point governing mobilization and eruption style
748 of rhyolitic magma. *Nature* 552, 235–238. <https://doi.org/10.1038/nature24488>

749 Di Genova, D., Romano, C., Alletti, M., Misiti, V., Scarlato, P., 2014a. The effect of CO₂ and
750 H₂O on Etna and Fondo Riccio (Phlegrean Fields) liquid viscosity, glass transition
751 temperature and heat capacity. *Chem. Geol.* 377, 72–86.
752 <https://doi.org/10.1016/j.chemgeo.2014.04.001>

753 Di Genova, D., Romano, C., Giordano, D., Alletti, M., 2014b. Heat capacity, configurational
754 heat capacity and fragility of hydrous magmas. *Geochim. Cosmochim. Acta* 142, 314–333.
755 <https://doi.org/10.1016/j.gca.2014.07.012>

756 Di Genova, D., Sicola, S., Romano, C., Vona, A., Fanara, S., Spina, L., 2017b. Effect of iron and
757 nanolites on Raman spectra of volcanic glasses: reassessment of existing strategies to
758 estimate the water content. *Chem. Geol.* 475, 76–86.
759 <https://doi.org/10.1016/j.chemgeo.2017.10.035>

760 Di Genova, D., Vasseur, J., Hess, K.-U., Neuville, D.R., Dingwell, D.B., 2017c. Effect of
761 oxygen fugacity on the glass transition, viscosity and structure of silica- and iron-rich
762 magmatic melts. *J. Non. Cryst. Solids* 470, 78–85.
763 <https://doi.org/10.1016/j.jnoncrysol.2017.05.013>

764 Di Genova, D., Zandona, A., Deubener, J., 2020b. Unravelling the effect of nano-heterogeneity
765 on the viscosity of silicate melts: Implications for glass manufacturing and volcanic
766 eruptions. *J. Non. Cryst. Solids* 545, 120248.
767 <https://doi.org/10.1016/j.jnoncrysol.2020.120248>

768 Dingwell, D.B., Courtial, P., Giordano, D., Nichols, A.R.L., 2004. Viscosity of peridotite liquid.
769 *Earth Planet. Sci. Lett.* 226, 127–138. <https://doi.org/10.1016/j.epsl.2004.07.017>

770 Dingwell, D.B., Hess, K.-U., Wilding, M.C., Brooker, R.A., Di Genova, D., Drewitt, J.W.E.,
771 Wilson, M., Weidendorfer, D., 2022. The glass transition and the non-Arrhenian viscosity
772 of carbonate melts. *Am. Mineral.* 107, 1053–1064. <https://doi.org/10.2138/am-2021-7752>

773 Dobson, D.P., Jones, A.P., Rabe, R., Sekine, T., Kurita, K., Taniguchi, T., Kondo, T., Kato, T.,
774 Shimomura, O., Urakawa, S., 1996. In-situ measurement of viscosity and density of
775 carbonate melts at high pressure. *Earth Planet. Sci. Lett.* 143, 207–215.
776 [https://doi.org/10.1016/0012-821X\(96\)00139-2](https://doi.org/10.1016/0012-821X(96)00139-2)

777 Douglas, R.W., Armstrong, W.L., Edward, J., Hall, D., 1965. A penetration viscometer. *Glas.*
778 *Technol.* 52–55.

779 Durben, D.J., McMillan, P.F., Wolf, G.H., 1993. Raman study of the high-pressure behavior of
780 forsterite (Mg₂SiO₄) crystal and glass. *Am. Mineral.* 78, 1143–1148.

781 Fei, H., 2021. Water Content of the Dehydration Melting Layer in the Topmost Lower Mantle.
782 *Geophys. Res. Lett.* 48, e2020GL090973.

783 <https://doi.org/https://doi.org/10.1029/2020GL090973>

784 Fukao, Y., Obayashi, M., 2013. Subducted slabs stagnant above, penetrating through, and
785 trapped below the 660 km discontinuity. *J. Geophys. Res. Solid Earth* 118, 5920–5938.
786 <https://doi.org/https://doi.org/10.1002/2013JB010466>

787 Ghosh, S., Schmidt, M.W., 2014. Melting of phase D in the lower mantle and implications for
788 recycling and storage of H₂O in the deep mantle. *Geochim. Cosmochim. Acta* 145, 72–88.
789 <https://doi.org/https://doi.org/10.1016/j.gca.2014.06.025>

790 Giordano, D., Russell, J.K., Dingwell, D.B., 2008. Viscosity of magmatic liquids: A model.
791 *Earth Planet. Sci. Lett.* 271, 123–134. <https://doi.org/10.1016/j.epsl.2008.03.038>

792 Gonnermann, H.M., Manga, M., 2013. Chapter 4: Dynamics of magma ascent in the volcanic
793 conduit, in: Fagents, S.A., Gregg, T.K.P., Lopes, R.M.C.E. (Eds.), *Modeling Volcanic*
794 *Processes: The Physics and Mathematics of Volcanism*. Cambridge University Press, pp.
795 55–84. <https://doi.org/10.1017/CBO9781139021562.004>

796 Hagy, H.E., 1963. Experimental Evaluation of Beam-Bending Method of Determining Glass
797 Viscosities in the Range 108 to 1015 Poises. *J. Am. Ceram. Soc.* 46, 93–97.
798 <https://doi.org/https://doi.org/10.1111/j.1151-2916.1963.tb11684.x>

799 Hennet, L., Cristiglio, V., Kozaily, J., Pozdnyakova, I., Fischer, H.E., Bytchkov, a., Drewitt,
800 J.W.E., Leydier, M., Thiaudière, D., Gruner, S., Brassamin, S., Zanghi, D., Cuello, G.J.,
801 Koza, M., Magazù, S., Greaves, G.N., Price, D.L., 2011. Aerodynamic levitation and laser
802 heating: *Eur. Phys. J. Spec. Top.* 196, 151–165. [https://doi.org/10.1140/epjst/e2011-01425-](https://doi.org/10.1140/epjst/e2011-01425-0)
803 [0](https://doi.org/10.1140/epjst/e2011-01425-0)

804 Hui, H., Zhang, Y., 2007. Toward a general viscosity equation for natural anhydrous and
805 hydrous silicate melts. *Geochim. Cosmochim. Acta* 71, 403–416.
806 <https://doi.org/10.1016/j.gca.2006.09.003>

807 Ishibashi, H., Sato, H., 2007. Viscosity measurements of subliquidus magmas: Alkali olivine
808 basalt from the Higashi-Matsuura district, Southwest Japan. *J. Volcanol. Geotherm. Res.*
809 160, 223–238. <https://doi.org/10.1016/j.jvolgeores.2006.10.001>

810 Karato, S., Karki, B., Park, J., 2020. Deep mantle melting, global water circulation and its
811 implications for the stability of the ocean mass. *Prog. Earth Planet. Sci.* 7, 76.
812 <https://doi.org/10.1186/s40645-020-00379-3>

813 Kawamoto, T., Holloway, J.R., 1997. Melting Temperature and Partial Melt Chemistry of H₂O-
814 Saturated Mantle Peridotite to 11 Gigapascals. *Science* (80-.). 276, 240–243.
815 <https://doi.org/10.1126/science.276.5310.240>

816 Keller, J., Krafft, M., 1990. Effusive natrocarbonatite activity of Oldoinyo Lengai, June 1988.
817 *Bull. Volcanol.* 52, 629–645. <https://doi.org/10.1007/BF00301213>

818 Kleest, C., Webb, S.L., Fanara, S., 2020. Rheology of melts from the colli albani volcanic district
819 (Italy): a case study. *Contrib. to Mineral. Petrol.* 175. [https://doi.org/10.1007/s00410-020-](https://doi.org/10.1007/s00410-020-01720-1)
820 [01720-1](https://doi.org/10.1007/s00410-020-01720-1)

821 Kohl, I., Bachmann, L., Mayer, E., Hallbrucker, A., Loerting, T., 2005. Glass transition in
822 hyperquenched water? *Nature* 435, E1–E1. <https://doi.org/10.1038/nature03707>

823 Kolzenburg, S., Di Genova, D., Giordano, D., Hess, K.-U., Dingwell, D.B., 2018. The effect of
824 oxygen fugacity on the rheological evolution of crystallizing basaltic melts. *Earth Planet.*
825 *Sci. Lett.* 487, 21–32. <https://doi.org/10.1016/j.epsl.2018.01.023>

826 Kono, Y., Kenney-benson, C., Hummer, D., Ohfuji, H., Park, C., Shen, G., Wang, Y., Kavner,
827 A., Manning, C.E., 2014. Ultralow viscosity of carbonate melts at high pressures. *Nat.*
828 *Commun.* 2–5. <https://doi.org/10.1038/ncomms6091>

829 Langhammer, D., Di Genova, D., Steinle-Neumann, G., 2021. Modelling the viscosity of
830 anhydrous and hydrous volcanic melt. *Geochemistry Geophys. Geosystems* n/a,
831 e2021GC009918. <https://doi.org/https://doi.org/10.1029/2021GC009918>

832 Langhammer, D., Steinle-Neumann, G., Di Genova, D., 2022. Modelling Viscosity of Volcanic
833 Melts with Artificial Neural Networks. *Geochemistry Geophys. Geosystems* 23.
834 <https://doi.org/10.1029/2022GC010673>

835 Li, J., Agee, C.B., 1996. Geochemistry of mantle–core differentiation at high pressure. *Nature*
836 381, 686–689. <https://doi.org/10.1038/381686a0>

837 Liebske, C., Behrens, H., Holtz, F., Lange, R.A., 2003a. The influence of pressure and
838 composition on the viscosity of andesitic melts. *Geochim. Cosmochim. Acta* 67, 473–485.
839 [https://doi.org/10.1016/S0016-7037\(02\)01139-0](https://doi.org/10.1016/S0016-7037(02)01139-0)

840 Liebske, C., Behrens, H., Holtz, F., Lange, R.A., 2003b. The influence of pressure and
841 composition on the viscosity of andesitic melts. *Geochim. Cosmochim. Acta* 67, 473–485.
842 [https://doi.org/10.1016/S0016-7037\(02\)01139-0](https://doi.org/10.1016/S0016-7037(02)01139-0)

843 Liebske, C., Schmickler, B., Terasaki, H., Poe, B.T., Suzuki, A., Funakoshi, K., Ando, R., Rubie,
844 D.C., 2005. Viscosity of peridotite liquid up to 13 GPa: Implications for magma ocean
845 viscosities. *Earth Planet. Sci. Lett.* 240, 589–604. <https://doi.org/10.1016/j.epsl.2005.10.004>

846 Lipman, P.W., Mullineaux, D.R., 1981. The 1980 eruptions of Mount St. Helens, Washington,
847 Professional Paper. <https://doi.org/10.3133/pp1250>

848 Loughlin, S.C., Vye-Brown, C., Sparks, R.S.J., Brown, S.K., Jenkins, S., 2015. Global volcanic
849 hazards and risk. Cambridge University Press, Cambridge.

850 Mahood, G.A., Hildreth, W., 1986. Geology of the peralkaline volcano at Pantelleria, Strait of
851 Sicily. *Bull. Volcanol.* 48, 143–172.

852 Mancini, M., Sendova, M., Mauro, J.C., 2021. Geometric analysis of the calorimetric glass
853 transition and fragility using constant cooling rate cycles. *Int. J. Appl. Glas. Sci.* 12, 348–
854 357. <https://doi.org/https://doi.org/10.1111/ijag.16073>

855 Mauro, J.C., Loucks, R.J., Gupta, P.K., 2009a. Fictive temperature and the glassy state. *J. Am.*
856 *Ceram. Soc.* 92, 75–86. <https://doi.org/10.1111/j.1551-2916.2008.02851.x>

857 Mauro, J.C., Yue, Y.Z., Ellison, A.J., Gupta, P.K., Allan, D.C., 2009b. Viscosity of glass-
858 forming liquids. *Proc. Natl. Acad. Sci. U. S. A.* 106, 19780–4.
859 <https://doi.org/10.1073/pnas.0911705106>

860 Meerlender, G., 1974. Viskositäts-Temperaturverhalten des Standardglases I der DGG. *Glas.*
861 *Ber.* 47, 1–3.

862 Mysen, B.O., 2014. Water-melt interaction in hydrous magmatic systems at high temperature
863 and pressure. *Prog. Earth Planet. Sci.* 1, 4. <https://doi.org/10.1186/2197-4284-1-4>

864 Mysen, B.O., Boettcher, A.L., 1975. Melting of a Hydrous Mantle: I. Phase Relations of Natural
865 Peridotite at High Pressures and Temperatures with Controlled Activities of Water, Carbon
866 Dioxide, and Hydrogen. *J. Petrol.* 16, 520–548. <https://doi.org/10.1093/petrology/16.1.520>

867 Mysen, B.O., Cody, G.D., 2005. Solution mechanisms of H₂O in depolymerized peralkaline
868 melts. *Geochim. Cosmochim. Acta* 69, 5557–5566.
869 <https://doi.org/10.1016/j.gca.2005.07.020>

870 Nakajima, A., Sakamaki, T., Kawazoe, T., Suzuki, A., 2019. Hydrous magnesium-rich magma
871 genesis at the top of the lower mantle. *Sci. Rep.* 9, 7420. <https://doi.org/10.1038/s41598-019-43949-2>

872

873 Nakajima, M., Stevenson, D.J., 2015. Melting and mixing states of the Earth’s mantle after the
874 Moon-forming impact. *Earth Planet. Sci. Lett.* 427, 286–295.

875 <https://doi.org/https://doi.org/10.1016/j.epsl.2015.06.023>

876 Ohtani, E., 1985. The primordial terrestrial magma ocean and its implication for stratification of
877 the mantle. *Phys. Earth Planet. Inter.* 38, 70–80.

878 [https://doi.org/https://doi.org/10.1016/0031-9201\(85\)90123-2](https://doi.org/https://doi.org/10.1016/0031-9201(85)90123-2)

879 Persikov, E.S., 1991. The Viscosity of Magmatic Liquids: Experiment, Generalized Patterns. A
880 Model for Calculation and Prediction. Applications, in: Perchuk, L.L., Kushiro, I. (Eds.),
881 *Physical Chemistry of Magmas*. Springer New York, New York, NY, pp. 1–40.

882 https://doi.org/10.1007/978-1-4612-3128-8_1

883 Persikov, E.S., Bukhtiyarov, P.G., Sokol, A.G., 2017. Viscosity of hydrous kimberlite and
884 basaltic melts at high pressures. *Russ. Geol. Geophys.* 58, 1093–1100.

885 <https://doi.org/10.1016/j.rgg.2017.08.005>

886 Pirrung, M., Fischer, C., Buchel, G., Gaupp, R., Lutz, H., Neuffer, F.-O., 2003. Lithofacies
887 succession of maar crater deposits in the Eifel area (Germany). *Terra Nov.* 15, 125–132.

888 Prescher, C., McCammon, C., Dubrovinsky, L., 2012. MossA: a program for analyzing energy-
889 domain Mössbauer spectra from conventional and synchrotron sources. *J. Appl. Crystallogr.*
890 45, 329–331. <https://doi.org/10.1107/S0021889812004979>

891 Richet, P., Lejeune, A.M., Holtz, F., Roux, J., 1996. Water and the viscosity of andesite melts.
892 *Chem. Geol.* 128, 185–197. [https://doi.org/10.1016/0009-2541\(95\)00172-7](https://doi.org/10.1016/0009-2541(95)00172-7)

893 Russell, J.K., Giordano, D., Dingwell, D.B., 2003. High-temperature limits on viscosity of non-
894 Arrhenian silicate melts. *Am. Mineral.* 88, 1390–1394.

895 Russell, J.K., Giordano, D., Dingwell, D.B., Hess, K.-U., 2002. Modelling the non-Arrhenian
896 rheology of silicate melts: Numerical considerations. *Eur. J. Mineral.* 14, 417–427.

897 <https://doi.org/10.1127/0935-1221/2002/0014-0417>

898 Scarani, A., Zandona, A., Di Fiore, F., Valdivia, P., Putra, R., Miyajima, N., Bornhöft, H., Vona,
899 A., Deubener, J., Romano, C., Di Genova, D., 2022. A chemical threshold controls
900 nanocrystallization and degassing behaviour in basalt magmas. *Commun. Earth Environ.* 3.
901 <https://doi.org/10.1038/s43247-022-00615-2>

902 Scherer, G.W., 1984. Use of the Adam-Gibbs equation in the analysis of structural relaxation. *J.*
903 *Am. Ceram. Soc.* 67, 504–511.

904 Schmandt, B., Jacobsen, S.D., Becker, T.W., Liu, Z., Dueker, K.G., 2014. Dehydration melting
905 at the top of the lower mantle. *Science* (80-.). 344, 1265–1268.

906 <https://doi.org/10.1126/science.1253358>

907 Sigurdsson, H., Carey, S., 1989. Plinian and co-ignimbrite tephra fall from the 1815 eruption of
908 Tambora volcano. *Bull. Volcanol.* 51, 243–270. <https://doi.org/10.1007/BF01073515>

909 Sigurdsson, H., Cashdollar, S., Sparks, R.S.J., 1982. The Eruption of Vesuvius in A. D. 79:
910 Reconstruction from Historical and Volcanological Evidence. *Am. J. Archaeol.* 86, 39–51.
911 <https://doi.org/10.2307/504292>

912 Sinmyo, R., Nakajima, Y., McCammon, C.A., Miyajima, N., Petitgirard, S., Myhill, R.,
913 Dubrovinsky, L., Frost, D.J., 2019. Effect of Fe³⁺ on Phase Relations in the Lower Mantle:
914 Implications for Redox Melting in Stagnant Slabs. *J. Geophys. Res. Solid Earth* 124,
915 12484–12497. <https://doi.org/https://doi.org/10.1029/2019JB017704>

916 Sinogeikin, S., Bass, J., Prakapenka, V., Lakshtanov, D., Shen, G., Sanchez-Valle, C., Rivers,
917 M., 2006. Brillouin spectrometer interfaced with synchrotron radiation for simultaneous x-
918 ray density and acoustic velocity measurements. *Rev. Sci. Instrum.* 77.
919 <https://doi.org/10.1063/1.2360884>

920 Sossi, P.A., Burnham, A.D., Badro, J., Lanzirrotti, A., Newville, M., O’Neill, H.S.C., 2020.

921 Redox state of Earth's magma ocean and its Venus-like early atmosphere. *Sci. Adv.* 6,
922 eabd1387. <https://doi.org/10.1126/sciadv.abd1387>

923 Stabile, P., Sicola, S., Giuli, G., Paris, E., Carroll, M. R., Deubener, J., Di Genova, D., 2021.
924 The effect of iron and alkali on the nanocrystal-free viscosity of volcanic melts: A
925 combined Raman spectroscopy and DSC study. *Chem. Geol.* 559, 119991.
926 <https://doi.org/10.1016/j.chemgeo.2020.119991>

927 Stagno, V., Stopponi, V., Kono, Y., Manning, C.E., Irifune, T., 2018. Experimental
928 determination of the viscosity of Na₂CO₃ melt between 1.7 and 4.6 GPa at 1200 –
929 1700 °C: Implications for the rheology of carbonatite magmas in the Earth's upper
930 mantle. *Chem. Geol.* 501, 19–25. <https://doi.org/10.1016/j.chemgeo.2018.09.036>

931 Stolper, E.M., 1982. Water in silicate glasses: An infrared spectroscopic study. *Contrib. to*
932 *Mineral. Petrol.* 81, 1-17 LA-English. <https://doi.org/10.1007/BF00371154>

933 Taniguchi, H., 1992. Entropy dependence of viscosity and the glass-transition temperature of
934 melts in the system diopside-anorthite. *Contrib. to Mineral. Petrol.* 109, 295–303.
935 <https://doi.org/10.1007/BF00283319>

936 Trots, D.M., Kurnosov, A., Ballaran, T.B., Tkachev, S., Zhuravlev, K., Prakapenka, V.,
937 Berkowski, M., Frost, D.J., 2013. The Sm:YAG primary fluorescence pressure scale. *J.*
938 *Geophys. Res. Solid Earth* 118, 5805–5813. <https://doi.org/10.1002/2013JB010519>

939 Vanden Poel, G., Istrate, D., Magon, A., Mathot, V., 2012. Performance and calibration of the
940 Flash DSC 1, a new, MEMS-based fast scanning calorimeter. *J. Therm. Anal. Calorim.* 110,
941 1533–1546. <https://doi.org/10.1007/s10973-012-2722-7>

942 Vanden Poel, G., Sargsyan, A., Mathot, V., Assche, G. V., Wurm, A., Schick, C., Krumme, A.,
943 Zhou, D., 2011. Recommendation for temperature calibration of fast scanning calorimeters
944 (FsCs) for sample mass and scan rate. *Beuth Verlag GmbH, Berlin Adam Met. vivo Vitri.*
945 *Investig. a nanostructured Coat. Mater. Preclin. study.* *Int J Nanomedicine* 9, 975–984.

946 Wade, J., Wood, B.J., 2005. Core formation and the oxidation state of the Earth. *Earth Planet.*
947 *Sci. Lett.* 236, 78–95. <https://doi.org/10.1016/j.epsl.2005.05.017>

948 Walker, G.P.L., Self, S., Wilson, L., 1984. Tarawera 1886, New Zealand — A basaltic plinian
949 fissure eruption. *J. Volcanol. Geotherm. Res.* 21, 61–78.
950 [https://doi.org/http://dx.doi.org/10.1016/0377-0273\(84\)90016-7](https://doi.org/http://dx.doi.org/10.1016/0377-0273(84)90016-7)

951 Weber, J.K.R., 2010. The Containerless Synthesis of Glass. *Int. J. Appl. Glas. Sci.* 1, 248–256.
952 <https://doi.org/https://doi.org/10.1111/j.2041-1294.2010.00026.x>

953 Whitfield, C.H., Brody, E.M., Bassett, W., 1976. Elastic moduli of NaCl by Brillouin scattering
954 at high pressure in a diamond anvil cell. *Rev. Sci. Instrum.* 47, 942–947.

955 Whittington, A.G., Hellwig, B.M., Behrens, H., Joachim, B., Stechern, A., Vetere, F., 2009. The
956 viscosity of hydrous dacitic liquids: implications for the rheology of evolving silicic
957 magmas. *Bull. Volcanol.* 71, 185–199. <https://doi.org/10.1007/s00445-008-0217-y>

958 Williams, Q., McMillan, P., Cooney, T.F., 1989. Vibrational spectra of olivine composition
959 glasses: The Mg-Mn join. *Phys. Chem. Miner.* 16, 352–359.
960 <https://doi.org/10.1007/BF00199555>

961 Xie, L., Yoneda, A., Katsura, T., Andraut, D., Tange, Y., Higo, Y., 2021. Direct Viscosity
962 Measurement of Peridotite Melt to Lower-Mantle Conditions: A Further Support for a
963 Fractional Magma-Ocean Solidification at the Top of the Lower Mantle. *Geophys. Res.*
964 *Lett.* 48, e2021GL094507. <https://doi.org/https://doi.org/10.1029/2021GL094507>

965 Xie, L., Yoneda, A., Yamazaki, D., Manthilake, G., Higo, Y., Tange, Y., Guignot, N., King, A.,
966 Scheel, M., Andraut, D., 2020. Formation of bridgmanite-enriched layer at the top lower-

967 mantle during magma ocean solidification. *Nat. Commun.* 11, 548.
968 <https://doi.org/10.1038/s41467-019-14071-8>
969 Xue, X., Kanzaki, M., 2004. Dissolution mechanisms of water in depolymerized silicate melts:
970 Constraints from ¹H and ²⁹Si NMR spectroscopy and ab initio calculations. *Geochim.*
971 *Cosmochim. Acta* 68, 5027–5057. <https://doi.org/10.1016/j.gca.2004.08.016>
972 Yue, Y.Z., Christiansen, J. deC., Jensen, S.L., 2002. Determination of the fictive temperature for
973 a hyperquenched glass. *Chem. Phys. Lett.* 357, 20–24. [https://doi.org/10.1016/S0009-](https://doi.org/10.1016/S0009-2614(02)00434-7)
974 [2614\(02\)00434-7](https://doi.org/10.1016/S0009-2614(02)00434-7)
975 Zandona, A., Groß, C.B.M., Rüdinger, B., Deubener, J., 2021. A threshold heating rate for
976 single-stage heat treatments in glass-ceramics containing seed formers. *J. Am. Ceram. Soc.*
977 104, 4433–4444. <https://doi.org/10.1111/jace.17822>
978 Zandona, A., Moustros, M., Genevois, C., Véron, E., Canizarès, A., Allix, M., 2022. Glass-
979 forming ability and ZrO₂ saturation limits in the magnesium aluminosilicate system.
980 *Ceram. Int.* 48, 8433–8439. <https://doi.org/10.1016/j.ceramint.2021.12.051>
981 Zandona, A., Patzig, C., Rüdinger, B., Hochrein, O., Deubener, J., 2019. TiO₂(B) nanocrystals in
982 Ti-doped lithium aluminosilicate glasses. *J. Non-Crystalline Solids X* 2, 100025.
983 <https://doi.org/10.1016/j.nocx.2019.100025>
984 Zheng, Q., Mauro, J.C., Ellison, A.J., Potuzak, M., Yue, Y., 2011. Universality of the high-
985 temperature viscosity limit of silicate liquids. *Phys. Rev. B - Condens. Matter Mater. Phys.*
986 83, 13–15. <https://doi.org/10.1103/PhysRevB.83.212202>
987 Zotov, N., Keppler, H., 1998. The influence of water on the structure of hydrous sodium
988 tetrasilicate glasses. *Am. Mineral.* 83, 823–834. <https://doi.org/10.2138/am-1998-7-814>
989